Tectonics

RESEARCH ARTICLE
10.1029/2019TC005832

Key Points:
- The Taltal fault system became active between 114 and 107 Ma, shortly after the end of brittle deformation on the Atacama fault system
- Older dates of structurally controlled intrusions and veining suggest that the Taltal fault system reactivated precursor structures
- The Taltal fault system records a shift from arc-parallel shear to E-W shortening and likely a change in early-Andean subduction dynamics

Supporting Information:
- Supporting Information S1
- Table S1
- Table S2
- Table S3
- Table S4
- Figure S1

Correspondence to:
S. P. Mavor,
skyler.mavor@colostate.edu

Citation:
Mavor, S. P., Singleton, J. S., Gomila, R., Heuser, G., Seymour, N. M., Williams, S. A., et al. (2020). Timing, kinematics, and displacement of the Taltal fault system, northern Chile: Implications for the Cretaceous tectonic evolution of the Andean margin. *Tectonics*, *39*, e2019TC005832. https://doi.org/10.1029/2019TC005832

Received 20 AUG 2019
Accepted 19 JAN 2020
Accepted article online 30 JAN 2020

Timing, Kinematics, and Displacement of the Taltal Fault System, Northern Chile: Implications for the Cretaceous Tectonic Evolution of the Andean Margin

S. P. Mavor[1], J. S. Singleton[1], R. Gomila[2], G. Heuser[2], N. M. Seymour[1], S. A. Williams[1], G. Arancibia[2], S. M. Johnston[3], A. R. C. Kylander-Clark[4], and D. F. Stockli[5]

[1]Department of Geosciences, Colorado State University, Fort Collins, CO, USA, [2]Departamento de Ingeniería Estructural y Geotécnica, Pontificia Universidad Católica de Chile, Santiago, Chile, [3]Physics Department, California Polytechnic State University, San Luis Obispo, CA, USA, [4]Department of Earth Science, University of California, Santa Barbara, CA, USA, [5]Department of Geological Sciences, The University of Texas at Austin, Austin, TX, USA

Abstract An extensive system of NW striking faults constitutes a major tectonic feature of the Coastal Cordillera in northern Chile, but fundamental questions remain about timing and kinematics of these structures. We present new geologic mapping and geochronology that provide insight into the structural evolution and tectonic significance of the Taltal fault system (TFS). The TFS displaces the Early Cretaceous arc-parallel Atacama fault system (AFS) with ~10.6 km cumulative offset across a ~15 km wide zone. Brittle fault data demonstrate that the TFS is vertical to steeply NE dipping with an average sinistral slip vector plunging 11° from the NW, compatible with E-W shortening. Two late Early Cretaceous dikes cut the AFS but are cut by TFS faults, and synkinematic calcite on a TFS strand yielded a U-Pb calcite date of 114.1 ± 7.0 Ma. These data demonstrate that the AFS was abandoned and deformation (re) initiated on the TFS between ~114–107 Ma, with continued slip after intrusion of the Tropezón (~110 Ma) and Librillo (106–101 Ma) plutonic complexes. Emplacement of a ~146 Ma rhyolite dike along the main Taltal fault and 141 ± 11 Ma calcite mineralization in the fault core suggests that a precursor structure influenced magma emplacement and fluid flow in the Late Jurassic/Early Cretaceous, supporting the hypothesis that the TFS reactivated long-lived inherited crustal weaknesses. The Early Cretaceous shift from arc-parallel shear to slip on the TFS and E-W shortening shortly preceded migration of the magmatic arc and records a change in the Chilean margin subduction dynamics.

1. Introduction

Tectonic activity in northern Chile has been dominated by subduction and arc magmatism since at least the Early Jurassic (e.g., Coira et al., 1982; Parada et al., 2007). In the Coastal Cordillera, plutons and volcanic deposits of the Jurassic to Early Cretaceous arc are dissected by an extensive system of NW striking sinistral faults from 25.4° to 27.2°S (Figure 1). Timing constraints suggest that some of these faults were active only in the Jurassic (Bonson, 1998; Contreras et al., 2013), whereas others clearly displace Early Cretaceous units. The largest magnitude sinistral displacement on an individual NW striking fault (7.5 km) occurs at the Taltal fault (Figures 1 and 2). The Taltal fault and nearby parallel faults (herein referred to as the Taltal fault system, TFS) displace the Atacama fault system (AFS), a major tectonic feature that traces more than 1,000 km north-south in the Coastal Cordillera and accommodated brittle-ductile sinistral shear in response to oblique convergence in the Early Cretaceous (Scheuber & Andriessen, 1990). The shift from slip on the AFS to TFS marks a notable change in deformation geometry and style near the active margin. While AFS deformation timing is well documented, the timing of slip on the TFS is largely unconstrained beyond its relative timing with the AFS. Evidence that AFS brittle deformation continued as late as ~110 Ma (Seymour et al., 2020) suggests that the most recently published 125–110 Ma age estimates for the younger Taltal fault (Espinoza et al., 2014) require revision.

The paleomagnetic studies suggest that NW striking faults in the Coastal Cordillera accommodated vertical-axis clockwise block rotation that cannot be fully explained by the development of the Bolivian orocline (Randall et al., 1996) and reveal that the Taltal fault is an important structural boundary that separates domains with a marked difference in tectonic rotations (Contreras, 2018). One kinematic model for clockwise rotation links NW striking faults to the transpressional Chivato fault system to form a crustal

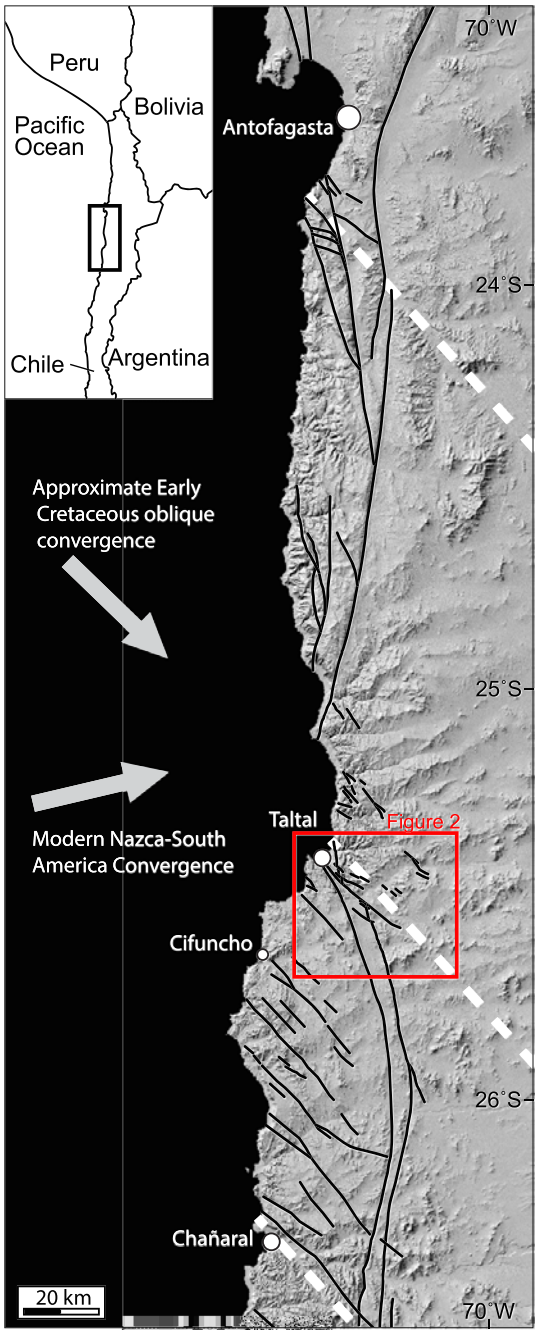

Figure 1. Digital elevation map of the Coastal Cordillera between 23° and 27°S, showing major regional faults (black). Structures not pertaining to the AFS or system of NW striking faults are omitted for clarity. Locations of faults are simplified from Álvarez et al. (2016), Cembrano et al. (2005), Escribano et al. (2013), and Grocott and Taylor (2002). The long-lived crustal weaknesses hypothesized by Abels and Bischoff (1999) are shown as dashed white lines. The modern Nazca-South America convergence direction is from Angermann et al. (1999), and an approximate Phoenix-South America oblique convergence direction is after Scheuber and Andriessen (1990).

sinistral strike-slip duplex in the Late Cretaceous after AFS abandonment (e.g., Grocott & Taylor, 2002; Randall et al., 1996; Taylor et al., 1998). According to this model, oblique convergence was largely partitioned between margin-parallel sinistral shear east of the AFS and margin-orthogonal shortening along NW striking faults in the Coastal Cordillera. Another tectonic model relies on kilometer-scale displacement of the Taltal fault during dextral transpression and rotation of large-scale domino blocks in the middle-late Eocene (Abels & Bischoff, 1999), yet it is unclear if the fault was active at that time.

Regionally, some NW striking faults are interpreted that wholly predate the AFS, whereas others postdate or evolved contemporaneously with the AFS (Bonson, 1998). Mapped relationships in the Jurassic La Negra Formation suggest that slip on NW striking sinistral faults near Cifuncho ceased in the Late Jurassic (Contreras et al., 2013). NW striking faults near Antofagasta are well documented as secondary faults that splay from and developed contemporaneously with AFS fault strands in a transtensional duplex arrangement (Cembrano et al., 2005; Jensen et al., 2011; Veloso et al., 2015). Northwest striking faults in the Precordillera have well-documented sinistral offset in the Eocene; however, an along-strike connection of these faults to the Taltal fault has been hypothesized but not demonstrated (Abels & Bischoff, 1999). While some TFS slip clearly postdates the AFS, the origin of the TFS and genetic relationship to parallel Jurassic faults are unclear. In addition, detailed kinematic data from the TFS and related NW striking faults in the Coastal Cordillera have not been published, so it is unclear to what extent this fault system records transpression or transtension. Here we present new geologic mapping and geochronology of units with prekinematic and synkinematic relationships to the TFS that constrain the slip history of the fault system, and we present brittle fault data that record the changing kinematic regime of the Cretaceous Chilean Coastal Cordillera.

2. Geologic Setting

The oldest rocks exposed in the Coastal Cordillera of northern Chile are late Paleozoic metasedimentary rocks of the Chañaral epimetamorphic complex. These rocks recorded multiple episodes of deformation during late Paleozoic subduction and terrane accretion (Bell, 1982; Fuentes et al., 2016). Triassic clastic strata overlying the Chañaral epimetamorphic complex record syndepositional extension and sedimentation patterns that suggest structural control by NW striking half-graben basins in northern Chile (Suarez & Bell, 1992; Tankard et al., 1995). Additional structurally controlled Triassic depocenters are widespread across central Chile and eastern Argentina (Charrier et al., 2007). The Andean orogenic cycle began by the Early Jurassic and in the early stages was characterized by arc-normal extension recorded by dikes and back-arc basin sedimentation (Charrier et al., 2007; Scheuber, 1994; Scheuber & Gonzalez, 1999). Southeast directed subduction oblique to the N-S trench imparted a sinistral margin-parallel shear component with some deformation recorded in the Early-Middle Jurassic and clearly recorded by the trench-linked AFS in the Early Cretaceous (Scheuber & Andriessen, 1990; Scheuber & Gonzalez, 1999). The AFS localized in the rheologically weak magmatic arc (Brown et al., 1993; Grocott et al., 1994), where elevated geothermal gradients near synkinematic plutons enabled ductile deformation at ~5–10 km crustal depths (Bonson, 1998; Seymour et al., 2020). Several ~139–119 Ma syntectonic plutons record the timing of ductile strain (e.g., Brown et al., 1993; Espinoza

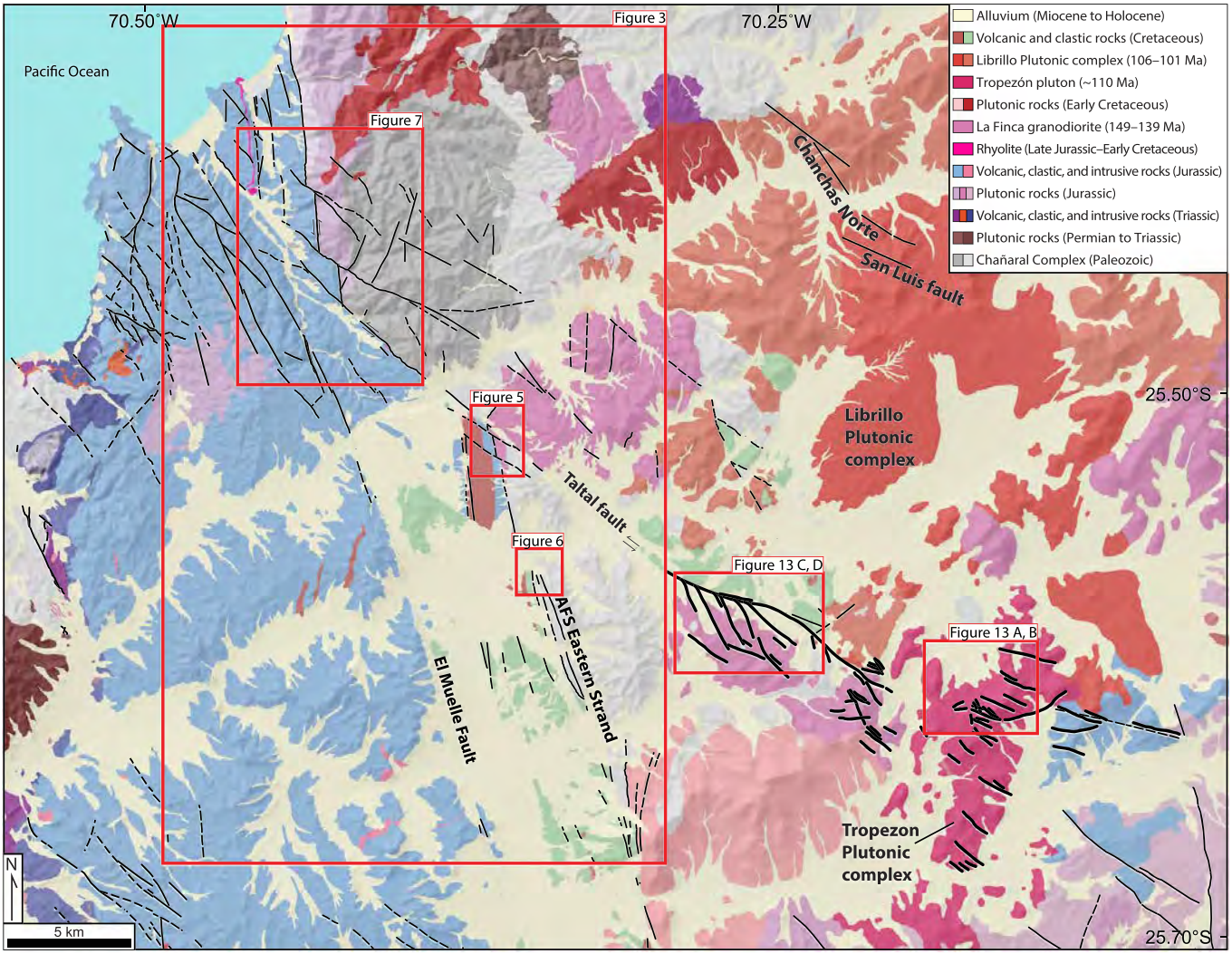

Figure 2. Compiled geologic mapping for the region near Taltal, Chile. Geology was compiled and simplified from 1:100,000 scale geologic maps (Contreras et al., 2013; Escribano et al., 2013; Espinoza et al., 2014). Bold black lines show our interpretation of distributed splay faults branching from the southeast end of the Taltal fault and cutting the ~110 Ma Tropezón pluton (magenta). These lineaments are mapped from aerial imagery, field reconnaissance, and lineaments in reduced to pole aeromagnetic data.

et al., 2014; Seymour et al., 2020; Wilson et al., 2000), which is overprinted by continued deformation in the brittle regime. Near the end of the Early Cretaceous, AFS deformation waned as arc magmatism migrated eastward from the Coastal Cordillera toward the present location in the high Andes (Dallmeyer et al., 1996; Scheuber et al., 1994), with a magmatic hiatus at ~90–80 Ma (Haschke et al., 2002). Recent work by Seymour et al. (2020) indicates that brittle slip on the AFS near Taltal was in its final stages at ~110 Ma. The AFS was subsequently cut and displaced by the TFS. Migration of the magmatic arc and residual cooling of the Coastal Cordillera coincides with the cessation of slip along the AFS (Brown et al., 1993; Seymour et al., 2020).

Late Cretaceous and Paleogene deposits are not preserved in the Taltal region. East of the Coastal Cordillera, Late Cretaceous volcanic rocks unconformably overlie folded Early Cretaceous deposits. Deformation and erosion associated with this angular unconformity is tied to the Peruvian phase of the Andean orogeny with regional crustal shortening and uplift (Scheuber et al., 1994), and basin deposits in the Precordillera record Peruvian phase deformation beginning as early as 107 Ma (Bascuñán et al., 2016). Additional margin-normal shortening events in the Cenozoic and development of the Bolivian orocline imparted a clockwise vertical-axis rotation to the Taltal region (Contreras, 2018).

Previous studies suggest that NW striking faults in the Coastal Cordillera occupy preexisting weaknesses inherited from Paleozoic contraction or Triassic rifting, both of which imparted a NW-SE structural grain. Collocation of these faults with linear magnetic anomalies suggests that they are situated on deep-seated weaknesses, and some studies suggest these faults are part of major crustal boundaries that extend as far as western Argentina (Abels & Bischoff, 1999; Bonson, 1998). NW striking sinistral faults near Cifuncho cut the lower but not upper members of the La Negra Formation, suggesting they were active in the early Late Jurassic (Contreras et al., 2013). The parallelism between these faults and the Taltal fault raises the possibility that parts of the TFS initiated in the Jurassic or earlier and were reactivated in the Cretaceous. However, parallelism of fault generations is considered equivocal criteria to establish fault reactivation (Holdsworth et al., 1997). Improved timing and kinematic constraints for the TFS are needed to determine how development of the TFS relates to the pre-Cretaceous structural grain, the end of AFS slip and migration of the magmatic locus, and Late Cretaceous to Cenozoic shortening events.

3. Previous Work

Reconnaissance geologic mapping by Arabasz (1968) recognized that the Taltal fault cuts and displaces the eastern strand of the AFS by ~10 km near the town of Taltal, and more recent estimates revise this displacement to ~8 km (Escribano et al., 2013). Limited fault plane orientation data collected by Arabasz (1971) indicate that TFS strands are near vertical to steeply northeast dipping. From the observation that the Taltal fault juxtaposes deeper-level Paleozoic metasedimentary rocks and plutons on the northeast side against shallow-level volcanic and volcaniclastic rocks to the southwest, previous workers have suggested a northeast-up reverse oblique component of slip on the Taltal fault (Escribano et al., 2013; Espinoza et al., 2014). However, detailed kinematic analyses including slickenline orientations that support this hypothesis have not been presented for the TFS.

Recent 1:100,000-scale mapping depicts the Taltal fault cross cutting the 106–101 Ma Librillo plutonic complex and also apparently cut by the older ~110 Ma Tropezón plutonic complex (Espinoza et al., 2014). This inconsistency also conflicts with the reported 125–110 Ma age range of the Taltal fault (Espinoza et al., 2014), bracketed between the end of AFS ductile deformation and intrusion of the Tropezón pluton. Descriptions of mine workings in the Tropezón and Librillo plutonic complexes suggest that both plutons are cut by faults (Escribano et al., 2013; Tornos et al., 2010), though these faults have not been tied to the TFS. Escribano et al. (2013) describe a small body of rhyolite along the Taltal fault that they interpret as Late Cretaceous and either postkinematic or synkinematic with the fault, though no direct geochronology of the rhyolite has been presented to test this hypothesis.

4. Methods

We mapped the TFS near its intersection with the AFS to clarify the timing and kinematic relationships between the TFS, AFS, and Cretaceous igneous units. Mapping was performed at 1:20,000 scale with key areas mapped at 1:10,000 scale and compiled and digitized using Esri ArcGIS 10.5.1 to align with the Esri world imagery basemap. We collected new high-resolution aerial imagery for key areas using a DJI Phantom 4 pro drone flown at altitudes <300 m above ground level. Photosets were processed in Agisoft Photoscan Pro to generate georeferenced orthomosaic images to support our field observations.

We collected fault-slip data from the Taltal fault and parallel strands, noting location, fault rock and mineralization, and confidence of slip-sense interpretation (Table S1 in the supporting information). Where offset markers were not directly visible in outcrop, sense of slip was determined using R- and T- fracture criteria (Petit, 1987), slickenfiber steps, asymmetric folding, or oblique foliation in fault gouge. Slip sense was assumed for some measurements either along strike from, or with similar geometry to, faults of known slip sense.

Structural data were analyzed using Stereonet 10.1.1 (Allmendinger et al., 2011; Cardozo & Allmendinger, 2013) and FaultKin 7.7.4 (Allmendinger et al., 2011; Marrett & Allmendinger, 1990) software. Orientation averages reported in the text are calculated using the maximum eigenvector. We determined incremental shortening and extension axes (*P* and *T* axes) for paired fault plane and slickenline lineation measurements (e.g., Marrett & Allmendinger, 1990), and cumulatively the mean axes reflect overall finite strain patterns.

4.1. Zircon U-Pb Geochronology and (U-Th)/He Thermochronology

We processed samples for zircon separation using standard magnetic and heavy liquid separation methods. Isotopic analytical data were collected with UTChron facilities at the University of Texas at Austin. Zircon U-Pb data were collected using laser ablation-inductively coupled plasma-mass spectrometry. Zircon grains were mounted parallel to the *c* axis on a tape mount and analyzed by a depth-profiling method. Data collection and reduction were performed following UTChron laboratory procedures outlined in Marsh and Stockli (2015) and Seymour et al. (2016) and errors propagated through data reduction. Unless stated otherwise, U-Pb dates referred to in the text are reported as mean $^{206}Pb/^{238}U$ dates $\pm 2\sigma$ uncertainty with grains filtered for <10% ($^{206}Pb/^{238}U$)/($^{207}Pb/^{235}U$) discordance calculated using the weighted mean calculation of Isoplot (Ludwig, 2003). Kernel density estimator plots are prepared using DensityPlotter software (Vermeesch, 2012) using the default optimal bandwidth calculated by the program. We employed single-grain zircon (U-Th)/He analysis following the methods of Wolfe and Stockli (2010) for one sample with insufficient zircon for a robust U-Pb analysis and probable xenocrystic zircon grains. Dates from such analyses represent the time at which the grains passed below the zircon He closure temperature of ~180–190 °C (Reiners et al., 2002, 2004; Wolfe & Stockli, 2010). Based on laboratory reproducibility of standards, an 8% analytical uncertainty is reported for each aliquot.

4.2. Calcite U-Pb Geochronology

The calcite-bearing fault surfaces with clear slip-sense indicators were sampled to directly date fault displacement using U-Pb calcite geochronology. Approximately 120 μm thick sections were prepared from samples cut perpendicular to the fault plane and parallel to the slip direction. Isotope analyses were performed on the thick sections using the University of California, Santa Barbara Dual laser ablation-inductively coupled plasma-mass spectrometry facility following the analytical procedures of Kylander-Clark et al. (2013) and Nuriel et al. (2017). For each investigated sample, calcite from a variety of textural settings within the mineralized portion of the fault was microsampled using an 85 μm spot run at 10 Hz for 15 s. Unknown analyses were corrected for instrument drift and mass bias using a combination of analyses from NIST614 glass and calcite standard WC-1 (254 Ma; Roberts et al., 2017) that were measured periodically throughout the analytical session. Given the variation in U-Pb ratios observed in most calcite samples, initial Pb compositions and dates can be calculated by regression of individual spot analyses on a Terra-Wasserburg diagram, and reported dates with 95% confidence errors are lower-intercept dates calculated using Isoplot (Ludwig, 2003). Low-U analyses with $^{238}U/^{206}Pb < 0.53$ that are inversely discordant have been removed from our preferred age calculations to avoid regression errors associated with potentially inherited or contaminant Pb, although inclusion of low-U analyses still yields ages that overlap within error of our preferred ages. Analyses of calcite standards ASH 15D (3.001 ± 0.012 Ma [2σ], Mason et al., 2013; Vaks et al., 2013) and Duff Brown (64.0 ± 0.7 Ma [2σ], Hill et al., 2016) analyzed throughout the analytical session yielded dates with 95% confidence errors of 3.14 ± 0.13 Ma and 66.4 ± 4.0 Ma, respectively, and that overlap within uncertainty of their accepted ages.

5. Distribution, Geometry, and Offset of TFS Faults

5.1. Map Relationships

All map-scale faults in the study area pertain to the NNW striking AFS or the younger NW striking TFS. The AFS is composed of two main NNW tracing faults ~5 km apart with intervening parallel subsidiary fault strands (Figure 3). The eastern strand of the AFS separates Paleozoic metasedimentary rocks and Mesozoic plutons east of the fault from Cretaceous andesites and volcaniclastic rocks west of the fault. The AFS eastern strand is near vertical and provides an excellent marker of horizontal offset across TFS faults. Mylonite zones up to 1.2 km thick and cataclasite zones up to 300 m thick are found only along the eastern strand, suggesting that this fault accommodated the most deformation and is the most significant strand of the fault zone. The western branch of the AFS juxtaposes Jurassic andesites against Cretaceous volcanic and clastic rocks with a gouge core and lacks mylonite or extensive cataclasite.

A prominent NNW to NW striking fault called El Muelle fault locally parallels both the AFS and TFS. The strike of the El Muelle fault changes from 344° near the intersection with the western branch of the AFS to 327° as it approaches parallelism with the Taltal fault, which likewise curves gently from strike 310° near the

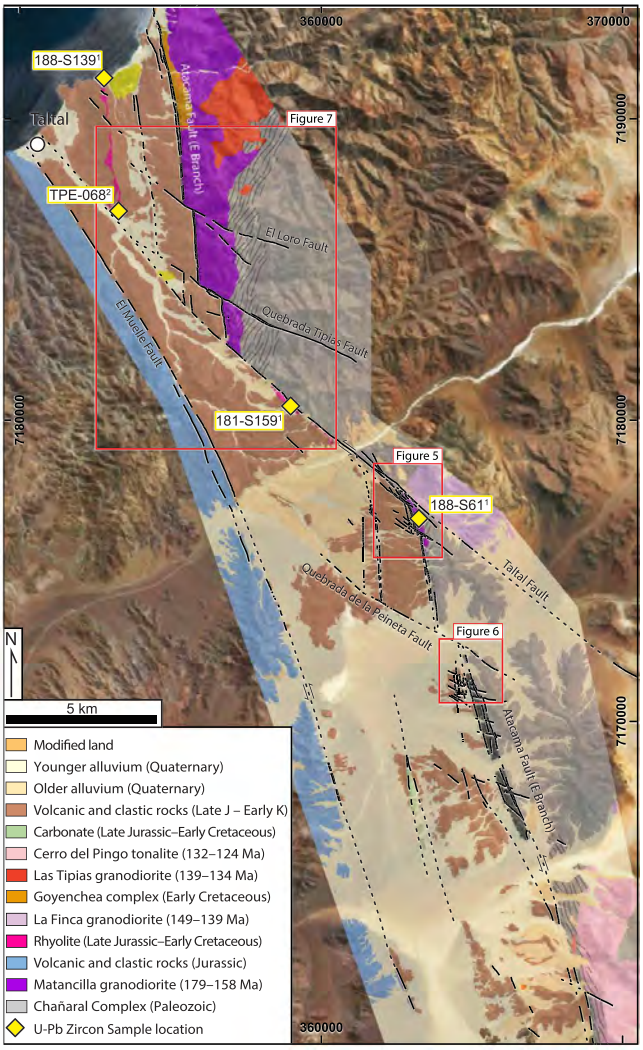

Figure 3. New geologic mapping of the Atacama and Taltal fault systems near Taltal, Chile. U-Pb zircon sample locations are marked with yellow diamonds. The rhyolite (pink) and Matancilla pluton (purple) offset markers across TFS faults are discussed in the text. Reference coordinates are given as WGS 1984 UTM zone 19S. Inset boxes give the locations of inset maps in Figures 5–7. U-Pb samples are from [1]this study and [2]Escribano et al. (2014).

intersection with the AFS to 320° near Taltal. Alluvium conceals the intersection zone of the El Muelle fault and AFS fault strands to the north with the AFS western branch, so it is unclear if the El Muelle fault splays from or is the direct continuation of the AFS western branch; we follow the nomenclature of Espinoza et al. (2014) to treat these faults separately. The El Muelle fault cuts Early Cretaceous volcanic rocks, but no postkinematic units have been identified. In contrast to other AFS fault strands, the El Muelle fault is not clearly displaced by the TFS.

Our geologic mapping identifies all exposed NW striking faults of the TFS that displace the Atacama fault by >10 m between 25.37°S and 25.70°S (Figure 3). Faults in the TFS are characterized by entirely brittle deformation with no evidence for associated mylonitic deformation. TFS fault damage zones exhibit brecciation but little cataclasite. Fault cores are instead composed of incohesive gouge and breccia, typically 5–10 m thick, which in several areas have eroded out to form fault-trace topographic lineaments (Figure 4). Immediately south of the Taltal fault, several closely spaced parallel faults displace the eastern strand of the AFS with tens to hundreds of meters of sinistral separation (Figure 5). South of Quebrada de la Peineta, numerous smaller faults offset the eastern strand of the Atacama fault with tens of meters of separation. We revise the mapping of Arabasz (1971) and Espinoza et al. (2014) to extend the NW striking fault at Quebrada de la Peineta into outcrop south of the Panamerican highway (Figures 3 and 6). This fault offsets the eastern strand of the AFS by ~990 m across the Quebrada de la Peineta. North of the Taltal fault, two major parallel faults displace the AFS (Figure 7). The Quebrada Tipias fault displaces the eastern strand of the AFS by 940 m and has a foliated fault gouge core that in places is up to 26 m thick (Figure 4). Near the intersection of the Quebrada Tipias fault and the AFS eastern strand, numerous centimeter-scale thickness calcite veins parallel the Quebrada Tipias fault and cross-cut AFS cataclasite. The northernmost TFS fault to displace the AFS is the El Loro fault, with 360 m sinistral separation of the AFS eastern strand (Figure 7). Using the near-vertical eastern strand of the AFS as a marker, we determine 7.5 km of offset on the main Taltal fault, and 10.6 km of cumulative offset for all TFS faults across a width of ~15 km (Figure 8).

5.2. Correlation of Units Across the Taltal Fault

5.2.1. Matancilla Pluton

At the intersection with the Taltal fault, the eastern strand of the AFS separates andesite on the west from granodiorite on the east (Figures 5 and 7). Previous mapping (Espinoza et al., 2014) depicted the thin strip of granodiorite east of the AFS and south of the Taltal fault as the La Finca pluton. However, when displacement across the TFS is restored, these outcrops are isolated from other outcrops of the La Finca pluton. We instead correlate this body with the Matancilla pluton, exposed east of the AFS north of Taltal. Restoration of the TFS aligns the outcrop east of Cerro Breadal to Matancilla granodiorite that intersects the Taltal fault from the north (Figures 3 and 7). Our new zircon U-Pb date of 169.0 ± 1.6 Ma from the southern strip of hornblende granodiorite (sample 188-S61, Figures 5 and 9, and Table S2) falls within the reported 175–158 Ma U-Pb zircon age range of the Matancilla pluton north of the Taltal fault (Escribano et al., 2013) and contrasts with the 149–139 Ma age range of the La Finca plutonic complex (Espinoza et al., 2014). This date supports the correlation across the Taltal fault indicated by field relationships and lithologic similarity.

5.2.2. Spherulitic Rhyolite

Following the hypothesis of Arabasz (1968), we correlate the pink spherulitic flow-banded rhyolite south of the Taltal fault (unit *Ksh* of Escribano et al., 2013) to the rhyolite exposed north of the Taltal fault just east of the town of Taltal (unit *Jmh*(*r*) of Escribano et al. (2013), Figures 2 and 7). Both units have a conspicuous pink

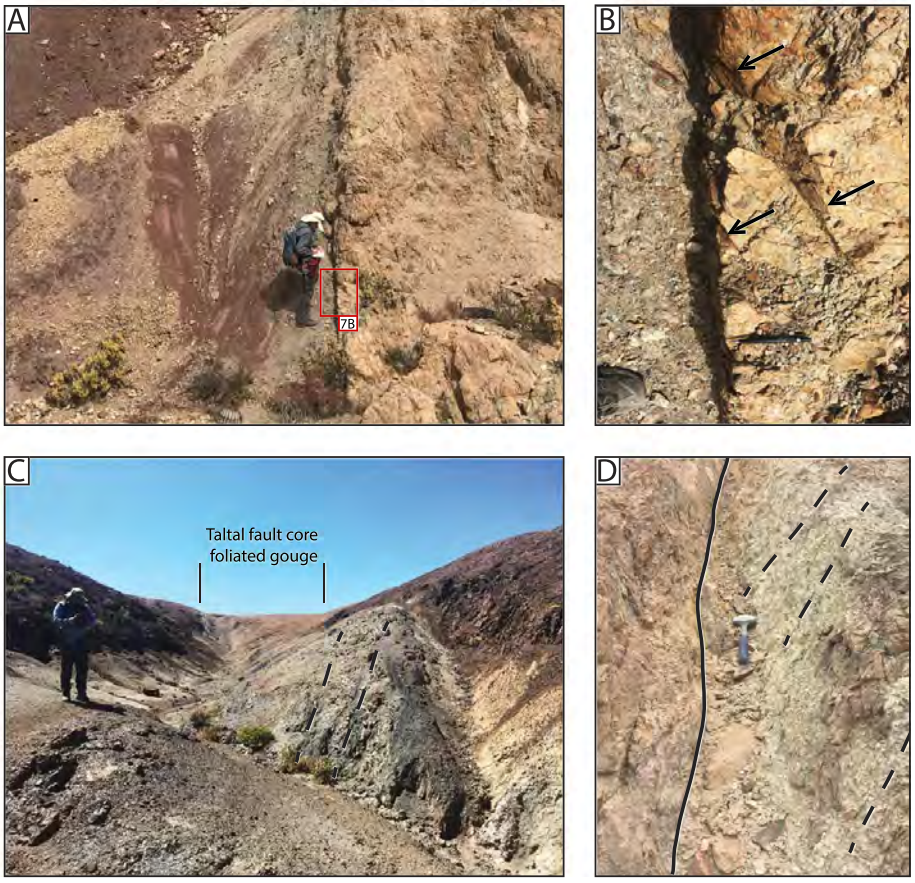

Figure 4. (a) Principal slip plane of the Taltal fault, separating Paleozoic metasedimentary rocks (right) from foliated fault gouge derived from spherulitic rhyolite. Photo taken ~600 m southeast of sample locality 181-S159, view to the northwest. (b) Detail view of the principal slip plane of the Taltal fault seen in 7A. Subsidiary fault surfaces with shallowly raking slickenlines are present on a sinistral Riedel shear adjacent to the principal slip plane (arrows). View from above, parallel to the NW-SE Taltal fault trace. Note pencil for scale. (c) Gouge core of the Taltal fault, with ~8 m of foliated gouge forming the less resistant fault trace valley. Gouge foliation (dashed lines) is oblique clockwise to the fault trace, indicating sinistral slip. Photo taken ~150 m northwest of sample locality 161-34, view to the southeast. (d) Foliated gouge in the core of the Quebrada Tipias fault. Gouge foliation (dashed lines) visible right of the rock hammer is oblique clockwise to the fault principal slip plane (solid line), indicating sinistral slip. View to the southeast.

color on fresh faces, millimeter-scale flow banding and are markedly distinct from the red-brown andesite and gray sandstone that are the dominant lithologies of the Mesozoic volcanic and sedimentary rocks in the region. Thin sections show well-developed radiating spherulites up to 3 mm in diameter with polygonal boundaries (Figure 10). Phenocrysts (4–15%) are dominantly alkali feldspar (3–7%, 1–3 mm), quartz (1–4%, 0.5–2 mm), red-brown euhedral biotite (1–2%, <1 mm), euhedral plagioclase (1-2%, <1 mm), and disseminated opaque grains (<0.5 mm). Quartz in samples from both outcrops has irregular embayment textures (Figure 10). The comparable proportions and sizes of phenocrysts, spherulitic texture, millimeter-scale flow banding, and marked lithologic difference with Jurassic and Cretaceous volcanic rocks typical of the region suggest that the rhyolite is a suitable offset marker across the Taltal fault.

North of the Taltal fault, the rhyolite forms resistant outcrops on a N-S ridge from Caleta el Hueso to the Taltal fault. Field relationships indicate that this rhyolite is a flow conformable in the surrounding sequence of andesite flows and volcaniclastic rocks, instead of a dike that intruded these rocks (e.g., Arabasz, 1971; Escribano et al., 2013). The upper and lower contacts of the rhyolite dip westward, concordant with bedding orientations in the surrounding volcaniclastic strata (Figure 7). Flow banding within the rhyolites is most commonly parallel to the contacts, but folded flow banding is visible in several outcrops, and measurements not parallel to the contacts have a seemingly random distribution (Figure 7). The lower contact of the flow is

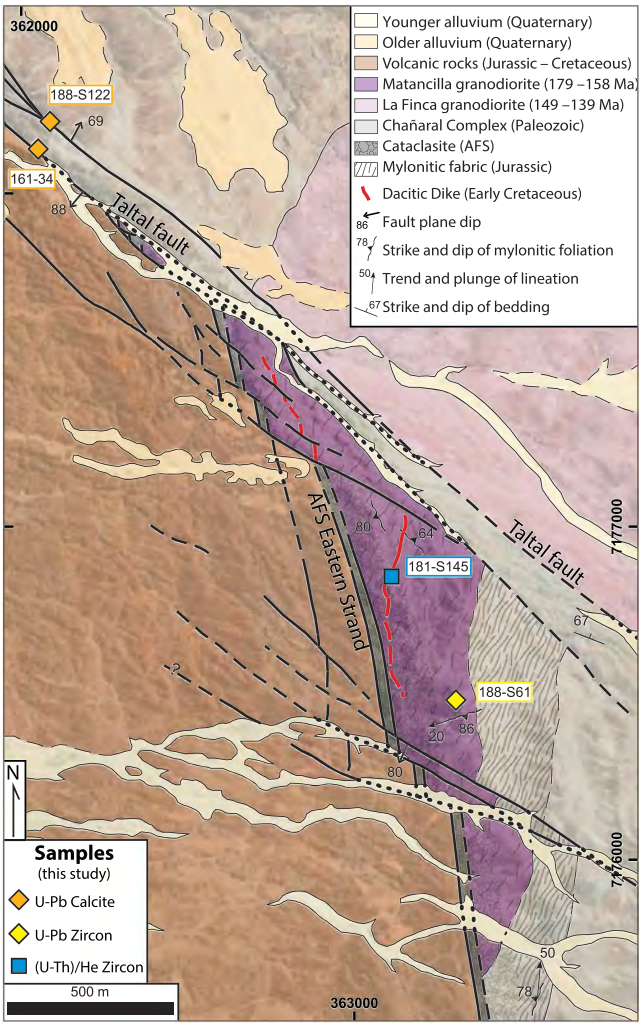

Figure 5. Geologic map of the intersection zone between the NNW-SSE striking AFS with the NW-SE striking Taltal fault showing the locations of samples analyzed in this study. Samples are symbolized by analytical method: yellow diamond, zircon U-Pb; orange diamond, calcite U-Pb; and blue square, zircon (U-Th)/He. Reference coordinates are given as WGS 1984 UTM zone 19S.

sharp against the underlying andesite, while the upper contact is marked by several meters of monomict rhyolite breccia that we interpret as flow-top autobreccia. Andesite flows and conglomerates overlying the rhyolite include rhyolitic clasts, clearly demonstrating that these strata postdate extrusion of the underlying rhyolite (Figure 10).

The southern rhyolite outcrops trace along the southern side of the Taltal fault for ~2.3 km, with the thickest exposure in the northwest end and a thinning tail extending southeast from this body (Figure 7). At the northeastern margin, the rhyolite is truncated by the Taltal fault and juxtaposed against Paleozoic metasedimentary rocks with ~10 m of fault gouge. The southwestern contact is not well exposed but traces roughly parallel to the Taltal fault and dips steeply. Flow banding measurements in these outcrops are most commonly subparallel with the Taltal fault (Figure 7), but folding is also visible at the outcrop scale. Volcaniclastic interbeds between andesite flows surrounding the rhyolite intrusion are shallowly dipping and are not rotated to parallelism with the Taltal fault. Foliation in Paleozoic metasedimentary rocks to the north consistently strikes northeast at a high angle to the Taltal fault, even within 3 m of the fault, suggesting that major fault-proximal rotation has not occurred. Where visible to the southwest of the Taltal fault, stratification in Mesozoic volcanic rocks is gently dipping. From these observations and the elongate outcrop pattern of rhyolite parallel to the Taltal fault, we interpret this rhyolite body to have intruded volcanic rocks on the southeastern side of the fault using the fault as a preferential pathway for magma flow. This intrusive rhyolite likely fed the surficial flows exposed north of the Taltal fault. Our interpretation follows that of Escribano et al. (2013) that intrusion of the southern rhyolite must have followed the Taltal fault or a precursor structure.

Sample 181-S159 was collected from a body of spherulitic rhyolite bound to the north by the Taltal fault (Figure 7). Of 55 grains analyzed for zircon U-Pb, a weighted mean average gives a date of 146.3 ± 0.8 Ma at <10% discordance (MSWD = 4.3) and 146.4 ± 1.7 Ma at <3% discordance (Mean Square of Weighted Deviates [MSWD] = 7.6, Figure 9 and Table S2). Sample 188-S139 was collected from coastal outcrops of flow-banded rhyolite at Caleta el Hueso (Figure 3). U-Pb zircon analyses of 50 grains give a weighted mean average of 143.6 ± 1.2 Ma at <10% discordance (MSWD = 10.7) and 144.7 ± 1.4 Ma at <3% discordance (MSWD = 8.0, Figure 9 and Table S2). The two sample dates overlap at 146.1–144.7 Ma when filtered to 3% discordance but do not overlap with a 10% discordance filter (Table S2). These dates contrast with a published date of 152.0 ± 2.8 Ma (zircon U-Pb SHRIMP; sample TPE-068 of Escribano et al., 2013) for the northern rhyolite body from a sample collected near the Taltal fault (Figure 7). However, each of the three dates have a relatively large spread of individual grain dates and high MSWD values for igneous samples, and the weighted mean date may not be the best representation of the true emplacement age of the rhyolite. Kernel density estimate plots of the three samples show overlapping spectra with one distinct peak for each sample (Figure 9).

Given the large spread of individual zircon dates in these rhyolite samples, we performed a *K-S* test comparison (Guynn & Gehrels, 2010) of the three samples following methods for detrital zircon analyses. These tests indicate that samples 181-S159 ($n = 55$) and 188-S139 ($n = 50$) are not statistically differentiable ($p = 0.069$ at <10% discordance and $p = 0.183$ at <5% discordance). With caveats noted that the *K-S* test is considered appropriate only for samples with ≥20 analyses and designed to compare samples with similar numbers of analyses (Guynn & Gehrels, 2010), we compared published zircon U-Pb analyses of sample TPE-068 ($n = 19$ via SHRIMP; Escribano et al., 2013) to the two rhyolite samples analyzed in this study. Both comparisons reject the null hypothesis and determine that sample TPE-068 (no discordance filter) is statistically

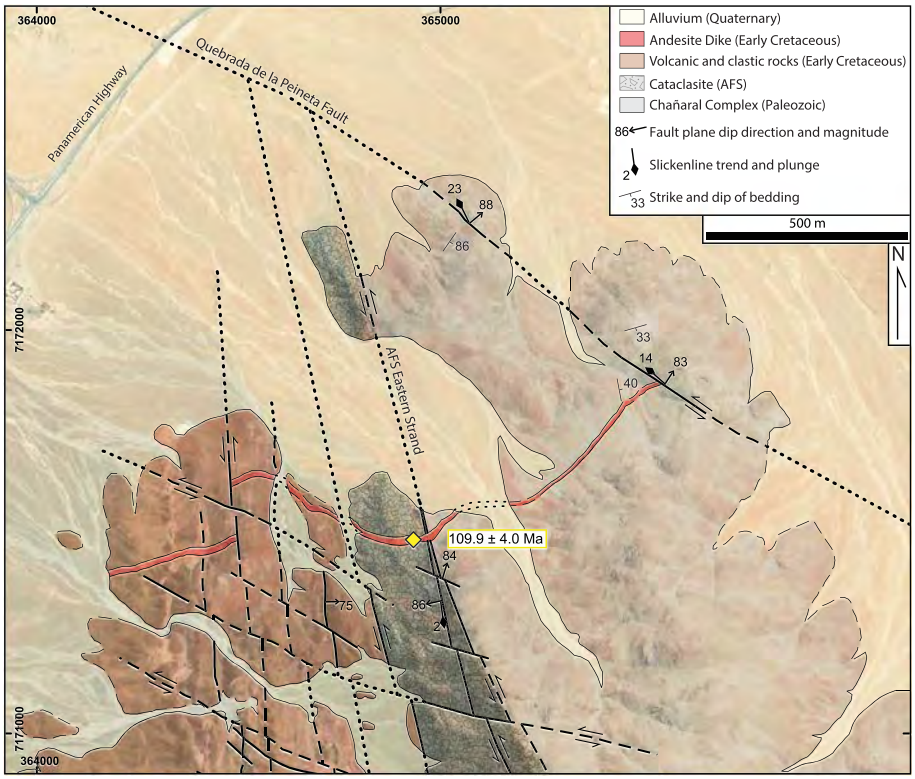

Figure 6. Geologic mapping of the andesitic dike in Quebrada de la Peineta (see also Seymour et al., 2020). The dike cuts the four strands of the AFS, including the easternmost (main) strand of the fault system, and is offset 148 m by a left-lateral AFS fault, indicating that slip shifted to westward strands as slip waned on the fault system. All AFS fault strands and the andesitic dike are cut and displaced ~990 m by the Quebrada de la Peineta fault. Yellow diamond marks the position of the zircon U-Pb sample presented by Seymour et al. (2020), dated to 109.9 ± 4.0 Ma. Reference coordinates are given as WGS 1984 UTM zone 19S.

different from samples 181-S159 (at <10% discordance, $p = 0.0005$) and 188-S139 (at <10% discordance $p = 0.00009$). Aside from a possible hiatus between individual flows, we have no compelling geologic reason why sample TPE-068 should have an age several million years different than its seemingly along-strike equivalent sample 188-S139 (Figure 3). The statistical difference between samples may instead reflect the discrepancy in the number of analyses or comparison across different analytical methods. Based on the lithologic similarity of all rhyolite outcrops and the results of the *K-S* test that show that the two rhyolite samples dated in this study via the same analytical method are not statistically dissimilar, we interpret the rhyolite as a satisfactory offset marker across the Taltal fault.

While field relationships suggest the southeastern rhyolite outcrops intruded at deeper levels than the northwestern counterpart outcrops, the magnitude of vertical separation cannot be resolved. The amount of horizontal offset required to juxtapose rhyolite outcrops across the Taltal fault is a minimum of 7.5 km and a maximum of 10.0 km. The eastern strand of the AFS is offset 7.5 km across the main strand of the Taltal fault and offset 0.9 km by the Quebrada Tipias fault. The northwestern extent of the Quebrada Tipias fault is concealed by alluvium, but it most likely merges with the Taltal fault (Figure 7). If the 8.4 km cumulative sinistral separation on these two faults is restored, the rhyolite north of the Taltal fault would align with the thickest part of the rhyolite exposure to the south; this reconstruction appears to be the most reasonable pre-TFS configuration. If the interpretation that the southern outcrop represents a deeper exposure level of the rhyolite is correct, it would indicate a component of NE down slip across these faults.

5.3. Kinematics

Measurements of the principal slip surface of the Taltal fault are vertical or dip steeply northeast (average principal slip plane is oriented 327, 80 NE; Figure 11). Slickenline lineations are generally shallowly

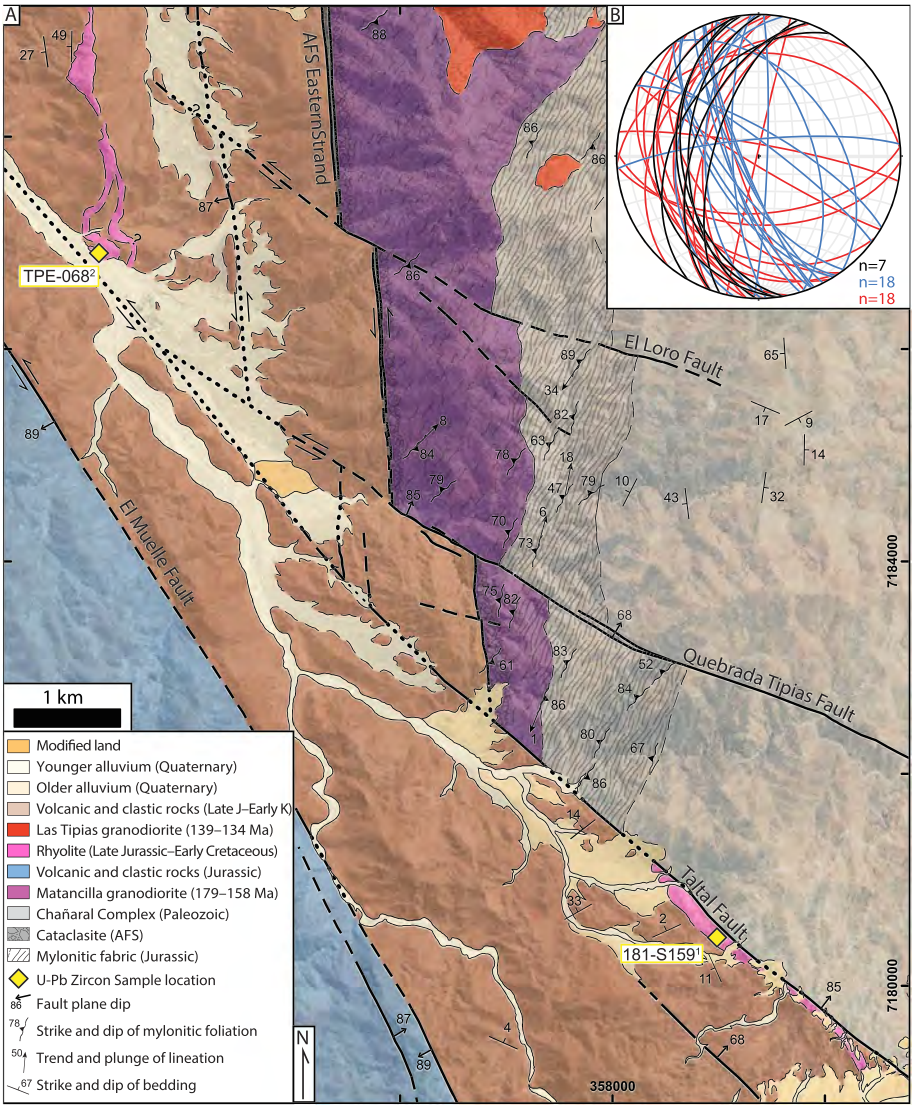

Figure 7. (a) Geologic mapping of the Taltal, Quebrada Tipias, and El Loro faults. The spherulitic rhyolite (pink) is an offset marker across the Taltal and Quebrada Tipias faults. Reference coordinates are given as WGS 1984 UTM zone 19S. U-Pb samples are from [1]this study and [2]Escribano et al. (2013). (b) Stereonet of flow banding in rhyolite. Flow banding north of the Taltal fault (red, $n = 18$) has many measurements parallel to bedding measured in overlying or underlying strata (black, $n = 7$). Flow banding measured in rhyolite outcrops south of the Taltal fault (blue, $n = 18$) is steeper and dominantly strikes NW-SE, roughly parallel to the Taltal fault.

raking, though sparse dip-slip lineations are observed. From measurements of all faults belonging to the TFS, the average fault plane is slightly steeper (309, 84 NE) and the average slickenline lineation plunges shallowly northwest (309/11). Kinematic indicators such as Riedel shears, T-fractures, and oblique gouge foliations (Figure 4) consistently indicate sinistral kinematics. We calculated a slip lineation perpendicular to the intersection of the average principal slip surface (315, 80°NE) and average gouge foliation (339, 74°E) following Moore (1978); this slip vector (319/17) has a slightly steeper northwest plunge than the average of slickenline lineation measurements (Figure 11). *P*- and *T*-kinematic axes for fault planes with slickenline lineations are oriented in shallow E-W and N-S clusters, respectively, with the average *P* axis shallowly west plunging (261/10). A fault plane solution from linked Bingham vector statistics gives a steeply northeast dipping nodal plane (309, 87°NE) and a shallowly northwest plunging slip lineation (309/08). These kinematic data indicate that TFS is a nearly pure strike-slip fault system with a slight NE down extensional component. These kinematics refute the interpretation that a reverse

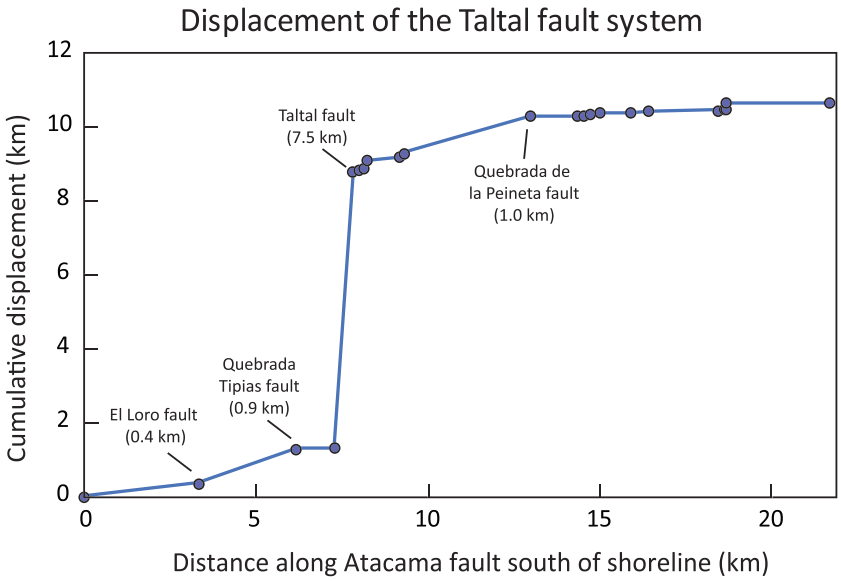

Figure 8. Cumulative sinistral offset of the Taltal fault system. Measurements use the near-vertical eastern strand of the AFS as an offset marker for horizontal separation. Faults are plotted as a function of the distance south from the shoreline north of Taltal along the AFS eastern strand. Individual displacements are marked for the largest faults.

component of oblique slip on the Taltal fault exhumed metasedimentary rocks of deeper crustal levels in the hanging wall (Escribano et al., 2013; Espinoza et al., 2014). Instead, we emphasize that this apparent difference of exposure levels is seen across the eastern strand of the AFS and was merely displaced by the Taltal fault (Figure 3).

Using the linked Bingham solution plane and slip lineation for the TFS and 7.5 km of measured sinistral horizontal separation, the Taltal fault records 990 m of NE down throw and 50 m of extensional heave. Using the linked Bingham solution plane and slip vector and 10.6 km of cumulative horizontal separation across all map-scale TFS faults, the cumulative NE-down throw is 1,390 m and the cumulative extensional heave is 70 m. Similar calculations made using the less steeply dipping average measured TFS fault plane and more steeply plunging average measured slickenline lineation give 2,040 m throw and 220 m heave for the entire fault system, and 1,450 m throw and 150 m heave for the Taltal fault alone.

While no suitable marker horizons exist to test these hypothesized dip-slip offset amounts, the component of NE down slip is consistent with the deeper exposure levels we interpret for the footwall rhyolite body. Furthermore, we note that the NW dipping contact between Chañaral complex metasedimentary rocks and the Matancilla pluton gives smaller amounts of horizontal separation across the Taltal and Quebrada Tipias faults than the amount of separation on the same faults using the AFS as a separation marker (Figure 7); this separation discrepancy can be accounted for by a component of NE down slip, resulting in deeper exposure level in the footwall.

5.4. Cross-Cutting Relationships and Geochronology Results

5.4.1. Dikes

In Quebrada de La Peineta southeast of Taltal a 7–12 m-wide porphyritic andesite dike cross cuts both the eastern strand of the AFS and a 175 m-wide zone of cataclasite bordering the eastern strand but is sinistrally displaced 148 m along an AFS strand 300 m further west (Figure 6, see also Seymour et al., 2020). These crosscutting relationships indicate that the dike intruded in the waning stages of AFS brittle deformation, after slip had ceased on the easternmost branches and shifted to an AFS strand further west. Both the dike and the AFS fault strands are offset by NW striking, steeply NE dipping faults with shallowly northwest raking slickenlines. From the similar geometry, kinematics, and cross-cutting relationships with the AFS we interpret this younger fault as part of the TFS. Seymour et al. (2020) present a 109.9 ± 4.0 Ma zircon U-Pb crystallization age of this dike, which serves to mark a transition between the latest stages of AFS deformation and later TFS faulting.

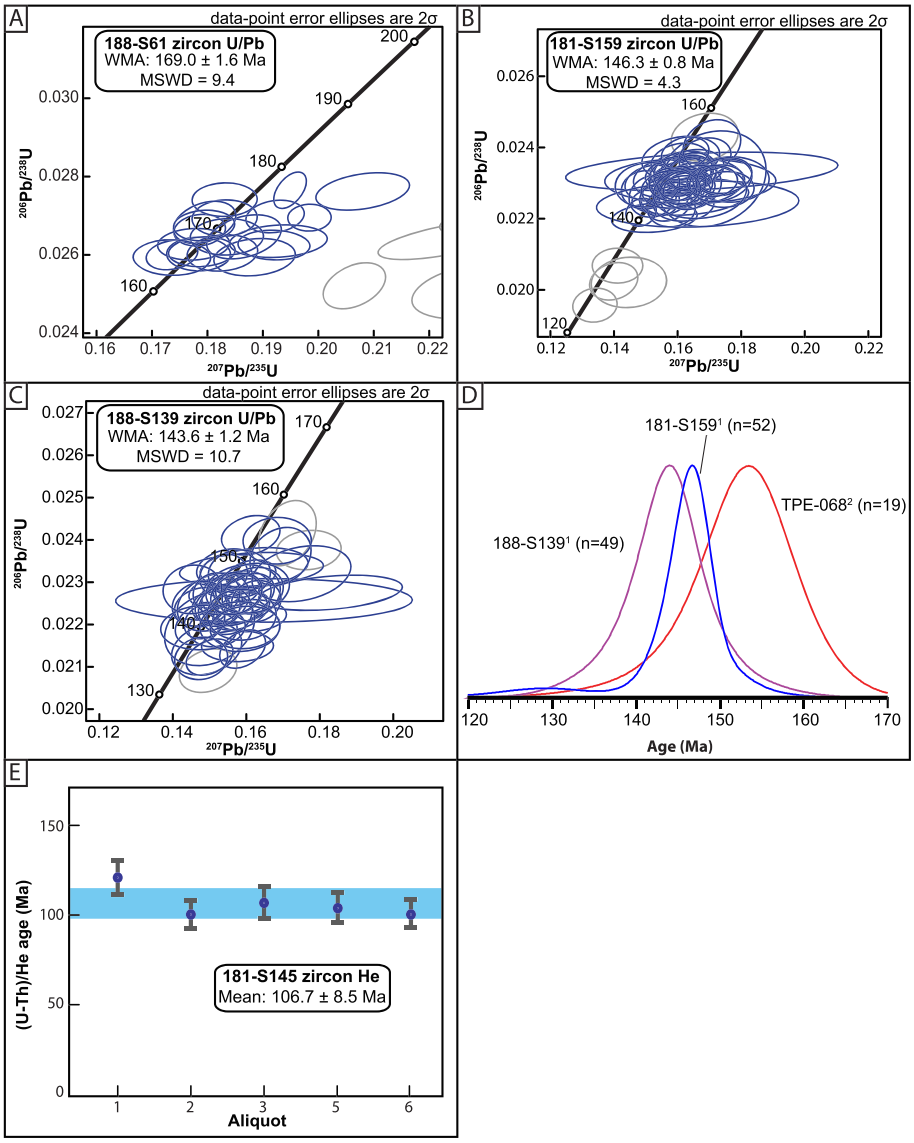

Figure 9. Geochronology analytical results. (a) U-Pb Concordia diagram of granodiorite sample 188-S61, showing a weighted mean age (WMA) of 169.0 ± 1.6 Ma from 27 total analyses. Seven grains of >10% discordance (shown in gray) are excluded from the weighted mean. This date is within the 175-158 age range of the Matancilla pluton (Escribano et al., 2013) and corroborates the lithologic correlation to that unit. (b) Zircon U-Pb concordia diagram of sample 181-S159 (55 analyses), showing a weighted mean age of 146.3 ± 0.8 Ma. Three grains are >10% discordant, and five grains are rejected from the WMA calculation (gray). While several younger grains (~125–132 Ma) are present in the sample, they are rejected as outliers from the weighted mean calculation algorithm. (c) Zircon U-Pb concordia diagram of sample 188-S139, showing a weighted mean age of 143.6 ± 1.2 Ma from 50 analyses, one grain >10% discordant is excluded, and three analyses are rejected from the WMA calculation (gray). (d) KDE plot of the three rhyolite U-Pb zircon samples, with overlapping age spectra. Sample analytical data are from: [1]this study (Table S2, filtered to <10% discordance) and [2]Escribano et al., 2013, not filtered for discordance). Peak heights are normalized to 100% of analyses. (e) Zircon (U-Th)/He cooling age of dike sample 181-S145 with a mean cooling age of 106.7 ± 8.5 Ma (blue highlight). Aliquot 4 gave a date older than the host pluton and is excluded.

Near the intersection of the eastern strand of the AFS and the Taltal fault, a 1–2 m wide dacitic dike cross cuts the AFS eastern strand cataclasite but is cut and displaced by several strands of the TFS (Figure 6). The magnitude of sinistral displacement of the dike is comparable to displacement of the eastern strand of the AFS across these faults (372 m across three map-scale faults). In addition, the dike is offset by numerous small faults with centimeter- to meter-scale offset; many of these faults are parallel to the Taltal fault and have

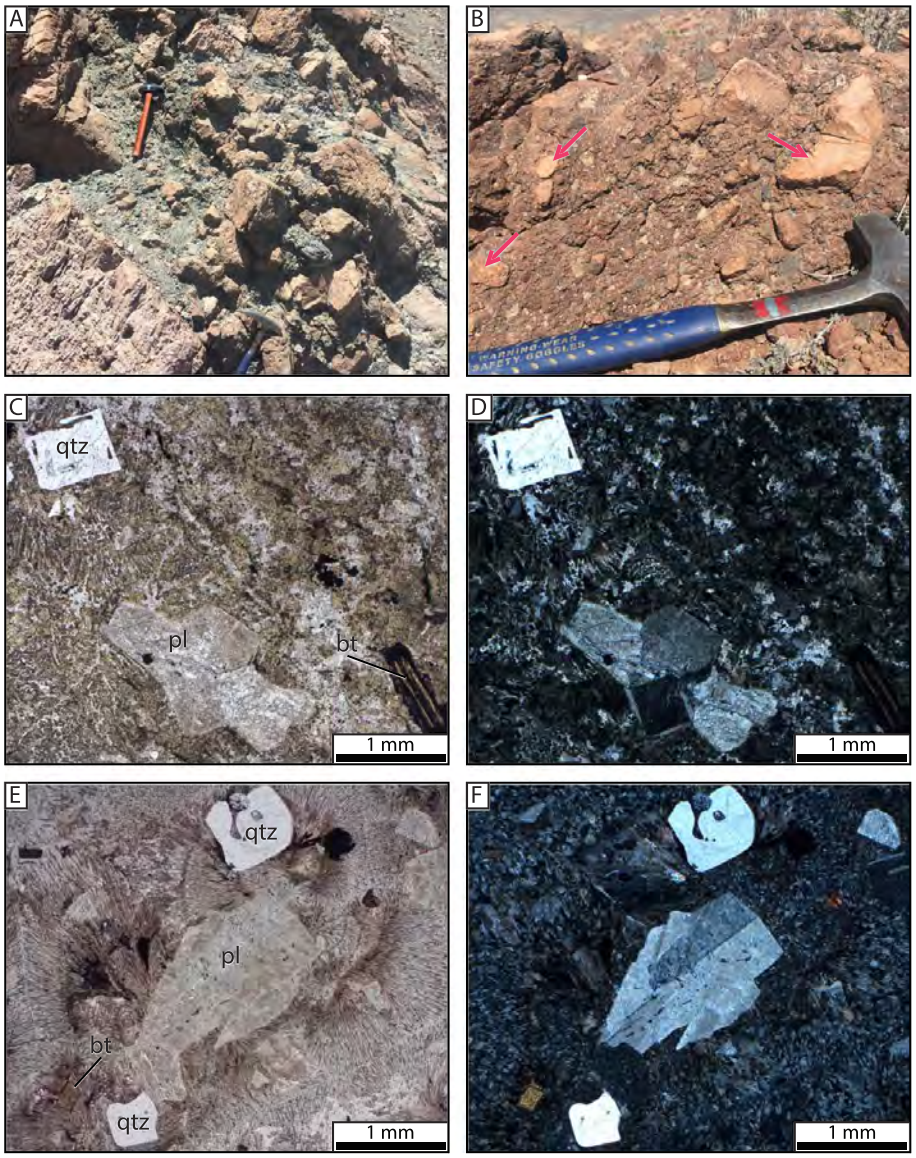

Figure 10. (a) Upper contact of the rhyolite unit near sample locality 188-S139. Rhyolite boulders are clasts in conglomerate with a dark green fine-grained clastic matrix. The boulder conglomerate interfingers along strike with sandstone and pebble conglomerate at the upper contact of the rhyolite flow. (b) Polymict conglomerate including clasts of spherulitic rhyolite (pink arrows) among clasts of porphyritic andesite and reworked sandstones. Photo taken 10 m upsection of the rhyolite flow upper contact. Rounded grains demonstrate surficial reworking of the rhyolite in the above strata. (c) Plane-polarized light photomicrograph of sample 181-S159. The spherulitic groundmass is largely composed of K-feldspar (yellow stain). Quartz (qtz), plagioclase (pl), and biotite (bt) phenocrysts are present. Quartz has irregular embayed grain shapes. (d) Cross-polarized light photomicrograph of sample 181-S159. (e) Plane-polarized light photomicrograph of sample 188-S139. Similar phenocryst assemblages and sizes, well-developed spherulitic texture, and embayed quartz texture demonstrate the lithologic similarity to sample 181-S159. Sample is unstained. (f) Cross-polarized light photomicrograph of sample 188-S139.

subhorizontal slickenlines and sinistral shear-sense indicators. Mineral separation for the dacitic dike sample 181-S145 yielded only six zircon grains. Given the likelihood that several or all of these grains are xenocrystic, producing a statistically sound U-Pb zircon crystallization age would be unlikely for this sample. Instead, we performed zircon (U-Th)/He analysis of this sample, which gives a date of 106.7 ± 8.5 Ma (Figure 9 and Table S3). This date is an average cooling age of five grains and records the time at which zircons cooled below ~180–190 °C, the closure temperature for the (U-Th)/He system (Reiners et al., 2002, 2004; Wolfe &

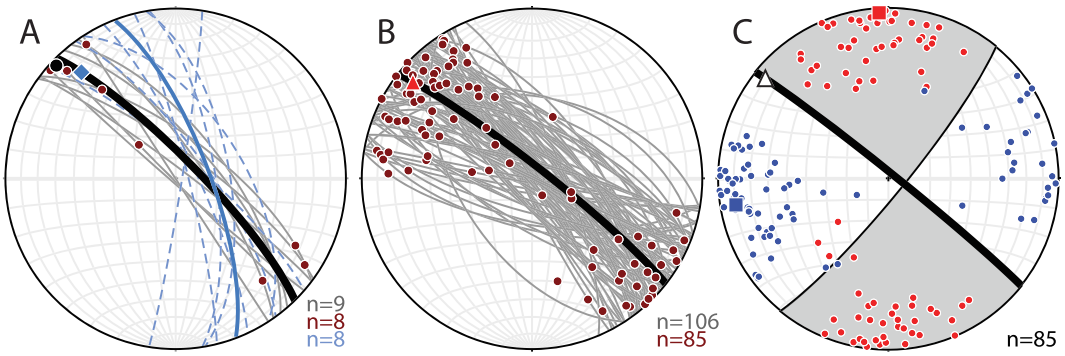

Figure 11. (a) Principal slip surface (gray) and slickenline lineation measurements (maroon circles) of TFS faults with >0.5 km sinistral displacement ($n = 9$). Measurements of foliated gouge ($n = 8$) in fault cores (dashed blue) are parallel or slightly oblique clockwise to principal slip surfaces and serve as a sinistral kinematic indicator. The average principal slip plane is oriented 315, 80°NE (black) and the average slickenline lineation is 314/04 (black circle). The blue diamond shows a calculated slip vector on the average principal slip surface plane perpendicular to the intersection with the average gouge foliation plane. (b) All TFS fault plane ($n = 106$) and slickenline lineation ($n = 85$) measurements. The average fault plane is in bold (308, 84°NE; maximum eigenvalue of poles to fault planes = 0.891), and the red triangle shows the average slickenline lineation plunging shallowly to the northwest (309/11, maximum eigenvalue = 0.751). (c) *P* axes (blue) and *T* axes (red) are shown for TFS fault planes with a measured slickenline lineation. The solution fault plane (309, 87°NE) dips steeply northeast and the slip vector (hollow triangle) plunges shallowly northwest (309/08). The average *P* axis (261/10, blue square) reflects an overall E-W shortening direction.

Stockli, 2010). Since the dike is at most 2 m wide it can be assumed to have rapidly cooled to ambient temperatures after emplacement, and the cooling age approximates the crystallization age of the dike. Alternatively, cooling below the zircon (U-Th)/He closure temperature may have lagged millions of years after dike emplacement if the country rocks were ≥ 180 °C. In this case, the date would record regional cooling as the magmatic arc migrated eastward in the Early Cretaceous, providing a minimum intrusion age of the dike. Regionally, zircon (U-Th)/He cooling dates in Jurassic plutons along the AFS are ~117–103 Ma (Ruthven et al., 2020; Seymour et al., 2020), so the dike cooling age is consistent with regional cooling. It is possible that heating via hydrothermal fluid flow fully or partially reset the zircon (U-Th)/He system postemplacement. However, given the similarity of the 106.7 ± 8.5 Ma cooling age to the ~110 Ma crystallization age of the late-AFS dike dated by Seymour et al. (2020), we favor the interpretation that the cooling age records intrusion of the dike during late stages of brittle deformation on the AFS.

5.4.2. Calcite Veining

Regionally, calcite veins represent late-stage mineralization with paragenetic textures indicating that calcite overprints or is coeval with hematite-chalcopyrite mineralization restricted to NW striking faults (Bonson, 1998). Along the AFS near its intersection with the TFS, we have observed several outcrops where calcite veins cut foliated gouge in the core of the eastern strand of the AFS. Calcite is also commonly associated with the TFS, supporting the interpretation that calcite mineralization is late stage with respect to the Early Cretaceous magmatic arc. Given that no bedrock map units are demonstrably younger than the Taltal fault, and that all dikes identified in this study are cut by the TFS, we employ U-Pb geochronology of calcite mineralization to constrain the timing of slip along the TFS.

5.4.2.1. Sample 188-S122

Near the Matancilla pluton, a subsidiary strand of the TFS cuts Chañaral complex metasedimentary rocks 90 m north of the Taltal fault (Figure 5). A pronounced NW-SE topographic lineament follows the gouge core of this fault strand, and fault planes within brecciated quartzite of the Chañaral epimetamorphic complex are exposed on either side. At sample locality 188-S122, calcite veins cut fault breccia (Figure 12). However, veins are themselves brecciated and in places offset by small faults with centimeter-scale sinistral separation. These relationships suggest that calcite veining was coeval with TFS brittle deformation. Petrographically, sample 188-S122 has calcite crystals >1 cm without pressure solution boundaries or slip surfaces on grain margins (Figure 12).

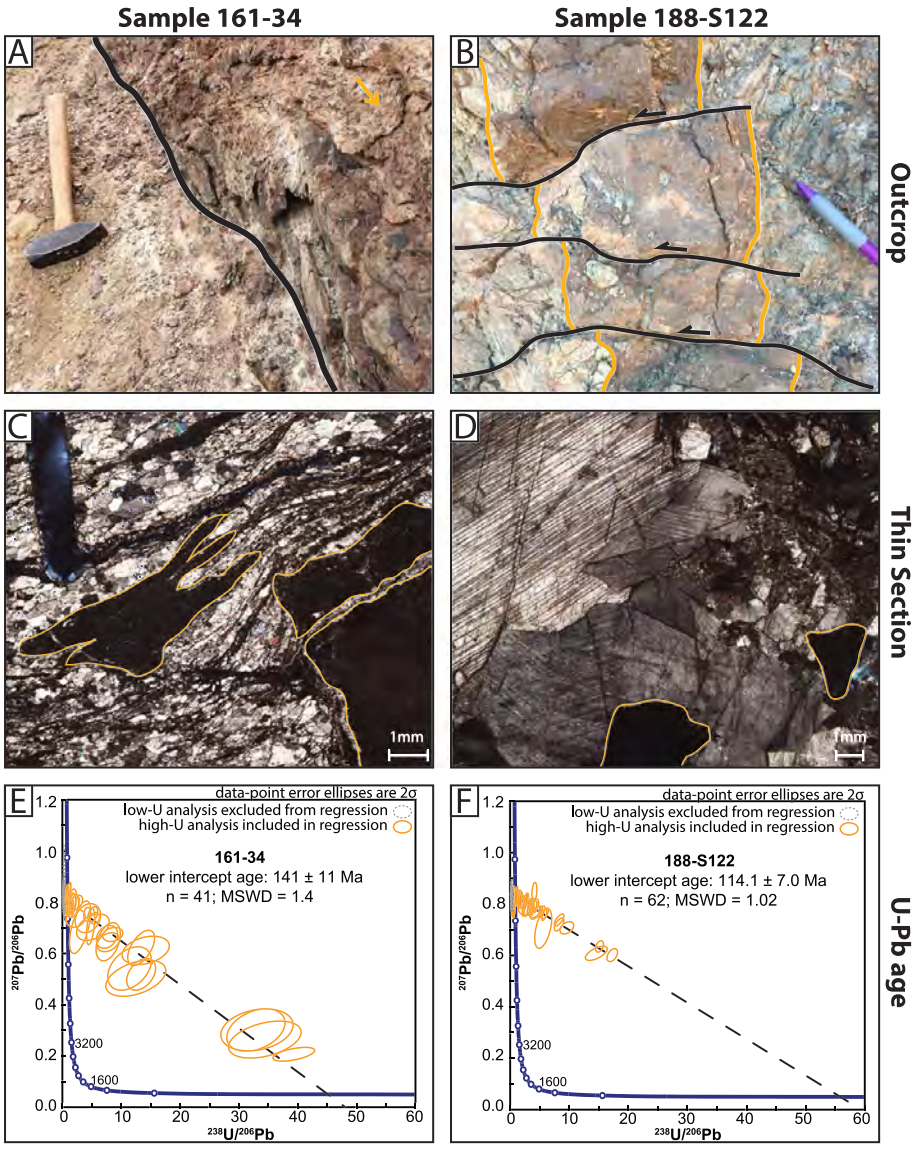

Figure 12. (a) Principal slip plane (bold line) of the Taltal fault at calcite sample location 161-34, separating incohesive fault gouge (left) from Paleozoic metasedimentary rocks (right). Calcite mineralization incorporating brecciated wall rock clasts is visible on subsidiary faults adjacent to the principal slip plane (orange arrow). View to the northwest. (b) 13 cm wide calcite vein (orange outline) at sample locality 188-S122. Calcite veining cuts fault breccia of a TFS fault but the vein displaced by sinistral faults with 1–3 cm offset. (c) Thin section (cross-polarized light) of calcite sample 161-34 showing grain boundary slip and pressure solution between calcite grains. Calcite deformation deflects around clasts of wall rock to the fault (orange outline). (d) Thin section of sample 188-S122, showing large (>1 cm) calcite grains without intragrain deformation and clasts of wall rock (orange outline). (e) U-Pb calcite concordia plot for sample 161-34. (f) U-Pb calcite concordia plot for sample 188-S122.

U-Pb isotopic analyses from distinct textural domains both adjacent to, and separated from, the wall rock yield a range of U concentrations that do not display any systematic correlation with their textural domain (Table S4). When high-U analyses from all textural domains are plotted on a regression line, they define a single population (MSWD = 1.02) with a lower-intercept age of 114.1 ± 7.0 Ma (113.2 ± 6.3 Ma including low-U analyses) that we infer represents the age of calcite precipitation (Figure 12 and Table S4).

5.4.2.2. Sample 161-34

Sample 161-34 was collected in the core of the Taltal fault along a subparallel secondary fault plane ~10 cm from the Taltal fault principal slip plane (Figure 12). Here the Taltal fault separates Paleozoic metasedimentary rocks from Mesozoic volcanic units to the south. Calcite in this sample has undergone brittle grain size

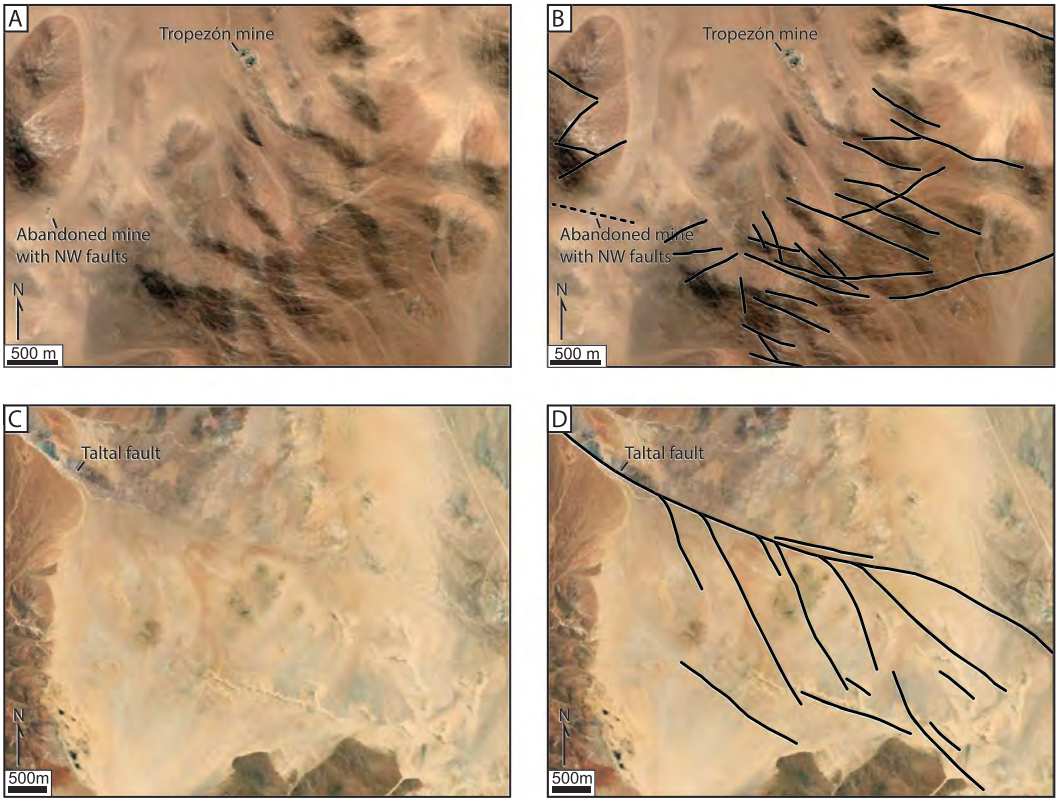

Figure 13. (a) Google Earth satellite imagery of the Tropezón pluton showing outcrops cut by abundant NW-SE and NE-SW striking lineaments. The abandoned mine discussed in the text exposes a mineralized NW-SE striking fault zone along strike with the Taltal fault and a lineament to the SE. (b) Esri aerial imagery of faults splaying from the southeastern extent of the Taltal fault. The Taltal fault is marked by a well-defined lineament in the northwest and curves gently eastward to a more E-W trace. NW-SE lineaments splay from the main fault trace. Poor outcrop and eolian cover prevent bedrock observations of the potential fault splays.

reduction along with scattered quartz grains and opaque minerals. Calcite mineralization has a deformation fabric defined by pressure solution boundaries and brecciated bands visible in thin section; this fabric wraps around a clast of metasedimentary wall rock (Figure 12). The pervasive grain-scale deformation in this sample indicates that this calcite mineralization records much, if not all, of the Taltal fault deformation and was early synkinematic to the fault.

U-Pb isotopic analyses from individual textural domains from this sample yielded a range of apparent calcite crystallization ages from 186 ± 52 Ma to 131 ± 10 Ma. The youngest and most radiogenic analyses from this sample are located within a 1 mm wide vein of calcite oriented parallel to but physically separated from the main calcite mineralization by a thin septum of wall rock. However, ages from all textural zones overlap within error, and when high-U analyses from all zones are combined on single regression line, the data define a single population (MSWD of 1.4) with an age of 141 ± 11 Ma (148 ± 11 Ma including low-U analyses) that is our preferred age for the timing of calcite precipitation in this sample (Figure 12 and Table S3).

5.4.3. Relationship of the TFS to the Tropezón and Librillo Plutonic Complexes

Based on the apparent lack of kilometer-scale offset of the Tropezón plutonic complex, Espinoza et al. (2014) suggest that Taltal fault slip had ceased by the time of that intrusion, dated to 110.0 ± 2.1 Ma (Tornos et al., 2010). However, this interpretation is inconsistent with mapping that depicts the Taltal fault displacing the 106–101 Ma Librillo plutonic complex (Espinoza et al., 2014). Google Earth imagery shows abundant NW-SE (and NE-SW) lineaments within the pluton south of the Tropezón mine (Figure 13); field-checked lineaments in this study are steep NW striking faults, some with calcite veining and shallowly plunging slickenlines. Abandoned mine workings 2.3 km southwest of the Tropezón mine expose NW-SE striking fault surfaces with Cu-oxide and calcite mineralization. Although this fault does not juxtapose lithologically

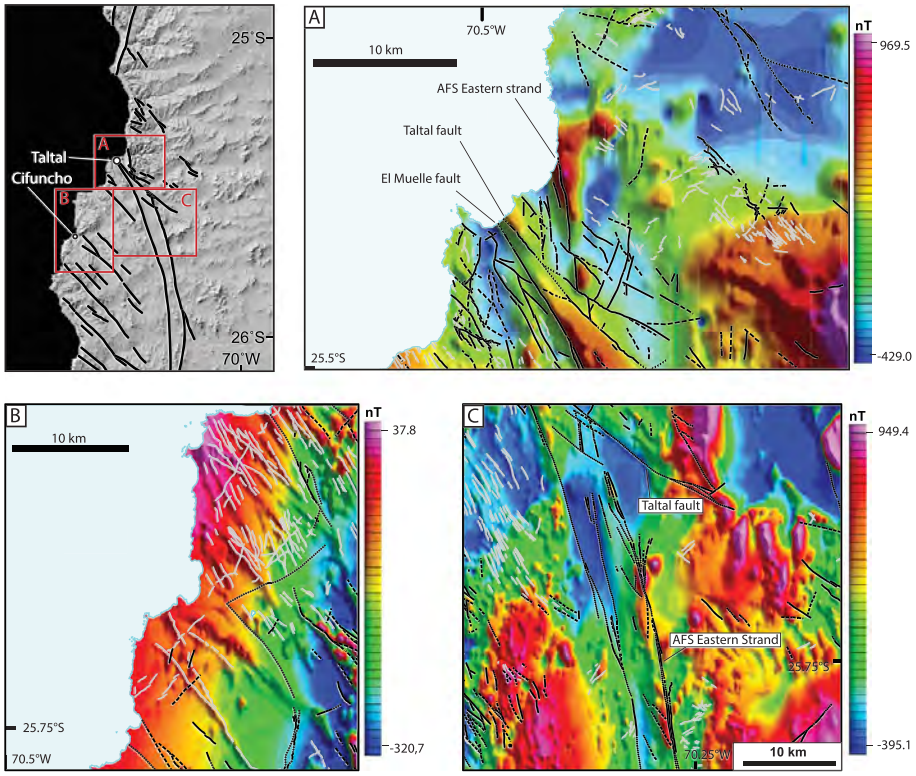

Figure 14. Reduced to pole aeromagnetic data in the Taltal region (modified from Vivallos & Donoso, 2014a, 2014b, 2014c). Faults (black) and dikes (gray) are compiled from 1:100,000 scale geologic mapping (Contreras et al., 2013; Escribano et al., 2013; Espinoza et al., 2014). (a) The Taltal and El Muelle faults show association with a strong NW-SE magnetic anomaly. (b) In the Cifuncho area, NW-SE tracing magnetic anomalies are collocated with mapped dikes and faults, both of Jurassic age (Contreras et al., 2013). This juxtaposition suggests that the nearby anomaly aligned with the Taltal fault could have an inherited component from Jurassic deformation and magmatism. (c) The magnetic anomaly associated with the NNW-SSE AFS appears to disrupt a more widespread NW-SE magnetic fabric, with a strong anomaly along the Taltal fault.

different map units, it is along strike with the trace of the Taltal fault located ~2.5 km northwest and could be a southeastern extension of the fault. Northwest striking lineaments that cut the southernmost outcrops of the Tropezón intrusive complex are visible in Google Earth imagery and reflected in reduced to pole aeromagnetic data (Figures 13 and 14; Vivallos & Donoso, 2014a, 2014b, 2014c). Similarly, NW striking faults (parallel to the Taltal fault) with shallow slickenline lineations cut the Librillo intrusive complex in other areas such as Mina San Juan (Bonson, 1998), where a nearby U-Pb zircon date gives a pluton crystallization age of 103.7 ± 1.9 Ma (Escribano et al., 2013). Further north, the Librillo intrusive complex is cut by the map-scale NW striking Raul Luis and Chanchas Norte faults with vertical or steep northeast dips near a sample with a 102.6 ± 2.4 Ma U-Pb zircon date (Figure 2, Escribano et al., 2013).

West of Mina Chuchufleta and south of Quebrada de la Peineta, the surface trace of the Taltal fault appears to bend, with the fault trace azimuth changing from 310° north of Quebrada de la Peineta to a more east-west trace as low as 285°. Near this bend in the fault trace, surface lineaments appear to splay from the Taltal fault and fan southward away from the arcuate trace of the Taltal fault (Figures 2 and 13). Similarly, other faults appear to splay northward from the Taltal fault; a fault splay depicted on several geologic maps (Arabasz, 1971; Naranjo & Puig, 1984; Ulriksen, 1979) branches to the north from the Taltal fault at Quebrada de la Peineta and traces into volcanic outcrops. Another fault splay traces from the Taltal fault north into mine workings at Mina Chuchufleta, where mineralization is described along fractures parallel to the Taltal fault (Bonson, 1998). Poor outcrop near the bend in the Taltal fault and a lack of contacts or marker horizons precludes determination of the amount of offset along these splays. However, each splay fault presumably accommodates strain that would otherwise be partitioned onto the main Taltal fault surface, and we hypothesize that offset along the main Taltal fault decreases southeastward. We propose that strain on the

southeastward extension of the Taltal fault is shared by this distributed network of faults and splays rather than a single through-going fault, and that map-scale displacement of pluton boundaries on any one fault is small enough to be hidden within the alluvial valleys that conceal outcrops of intrusive contacts. Thus, the Tropezón intrusive complex does not give a map-scale appearance of offset along the Taltal fault but on closer inspection does appear to be cut by numerous NW-SE faults. Although the magnitude of shear in these plutonic complexes cannot be summed, it appears unlikely that the full offset of TFS displacement observed to the west is recorded by these plutons. If this interpretation is correct, it follows that the Tropezón and Librillo intrusive complexes intruded during TFS deformation and are offset by the TFS by lesser amounts than earlier-formed units.

6. Discussion

6.1. Structural Inheritance of the TFS

If the pre-TFS crust were isotropic, an equal distribution of conjugate sinistral and dextral faults (or thrust faults) might be expected to form in response to E-W shortening. Instead, post-AFS Cretaceous deformation is accommodated only by NW striking sinistral faults; the near absence of dextral faults and thrust faults coeval with the TFS suggests a component of pre-Cretaceous structural inheritance that favored NW striking faults. Multiple deformation episodes in the pre- or early-Andean tectonic history of the region created anisotropy that could serve as loci for later fault localization. The Chañaral epimetamorphic complex and Chañaral mélange are characterized by a NW-SE trending structural grain most likely associated with NE directed subduction during the late Paleozoic (Bell, 1984, 1987). The mélange facies south of Cifuncho have NW trending chevron folds, and the adjacent Paleozoic metasedimentary rocks to the east have a NW-SE structural fabric defined by SE vergent thrusts and thrust-related folds (Fuentes et al., 2016). NW striking extensional faults appear to have controlled sedimentation as early as the Triassic (Suarez & Bell, 1992; Tankard et al., 1995). Such structures could have produced a preexisting anisotropy favorable for reactivation by the TFS.

Contreras (2018) demonstrates that paleomagnetic clockwise rotations are greater in rocks south of the Taltal fault with pre-Late Jurassic magnetization than in rocks with Early Cretaceous magnetization and suggests that a Late Jurassic-Early Cretaceous clockwise rotation event was accommodated by domino fault-block rotation of NW striking faults southeast of Taltal, perhaps kinematically linked with early activity of the AFS. Bonson (1998) described the Taltal fault as collocated with a strong gradient in reduced to pole aeromagnetic data. We note that more recent aeromagnetic data (Vivallos & Donoso, 2014a) support the observation that the Taltal fault is sited along an aeromagnetic lineament, even in areas where the same map unit is juxtaposed across the fault at the surface (Figure 14). This observation suggests that the geophysical lineament reflects a deep-seated structure. South of Taltal, aeromagnetic and topographic data show a dominant NW-SE grain. Contreras et al. (2013) describe a system of NW-SE faults in this area with Middle Jurassic ages. The similar orientations of these structures to TFS faults and alignment with strong aeromagnetic lineaments (Figure 14) support the interpretation that TFS faults occupy pre-Cretaceous weaknesses of earlier-formed structures. Prinz et al. (1994) describe an abrupt change in the thicknesses of Bathonian and Oxfordian strata across a NW-SE lineament that appears to align with the southeastern projection of the Taltal fault. They interpret this relationship to record fault activity on this lineament since at least the Jurassic and note that other changes in Triassic to Late Jurassic sediment thickness align with the major NW-SE lineaments across northern Chile and northwestern Argentina described by Salfity (1985). We consider this relationship strong evidence for significant pre-AFS displacement along NW striking structures that served as precursors for TFS faulting.

The 141 $\pm$ 11 Ma age of calcite mineralization along the Taltal fault (sample 161-34) indicates the presence of a fluid pathway at that time. Deformation of calcite visible in thin section is likely a result of later sinistral slip on the Taltal fault. We propose that the rhyolite intrusion exposed for ~2 km on the southeast margin of the Taltal fault utilized the proto-Taltal fault structure as a conduit for magma flow. If true, the ~146 Ma age of this rhyolite corroborates the calcite data to show the presence of a preexisting NW striking structure in the Late Jurassic to Early Cretaceous.

While the above lines of evidence argue that the TFS faults occupy preexisting weaknesses, we do not find compelling evidence for measurable pre-AFS strike-slip displacement across the Taltal fault. The intrusive

contacts of the 175–158 Ma Matancilla pluton and the 149–139 Ma La Finca pluton into the surrounding metasedimentary rocks do not record lateral offset greater than the offset measured on the eastern strand of the mid-Early Cretaceous AFS. This observation suggests that either there was no displacement on the proto-Taltal fault within that timeframe, or that there may have been dip-slip displacement that cannot be resolved by using these near-vertical offset markers. The latter interpretation is more consistent with the changes in sedimentary thickness described by Prinz et al. (1994).

TFS faults with the greatest offset are centered near the Taltal fault. NW striking faults are not present north of the El Loro fault, and south of Quebrada de la Peineta TFS faults have relatively minor magnitudes of displacement. NW striking faults are ubiquitous south of Taltal to at least 27°S (Bonson, 1998), but no single fault offsets the AFS with displacement rivaling the 7.5 km of the Taltal fault. We propose that the distribution of TFS faulting is a result of suitably oriented and mechanically weak preexisting zone centered on the Taltal fault, such that post-AFS fault displacement was preferentially localized on this inherited structure zone.

6.2. Timing of the TFS

The two Cretaceous dikes observed in this study are cut by the TFS, including two dikes that were emplaced following or at the very end of AFS slip. These dikes, with dates of 106.7 ± 8.5 Ma (zircon (U-Th)/He) and 109.9 ± 4.0 Ma (zircon U-Pb, Seymour et al., 2020), confirm the hypothesis that the brittle AFS was active until at least ~114 Ma and perhaps as late as ~106 Ma (the limits of uncertainty of the latter dike), and the requisite stress regime to shift slip to TFS faults had not yet been established. The amount of offset of dike 181-S145 across strands of the TFS is comparable to the amount of offset of the AFS eastern strand along the same faults, suggesting that the TFS was not active when this dike intruded. However, while the 106.7 ± 8.5 Ma zircon (U-Th)/He cooling age may represent the time of dike emplacement, it could also reflect regional cooling and thus gives only a conclusive minimum age.

While we have no direct offset measurements of TFS faults that cut the Tropezón plutonic complex (110.0 ± 2.1 Ma, Tornos et al., 2010), it appears likely that the amount of the cumulative offset on these faults is less than the 7.5 km of offset on the Taltal fault further east. This interpretation is consistent with the 114.1 ± 7.0 Ma U-Pb calcite date that demonstrates that TFS faults had already accumulated slip and developed gouge fault cores by the time the Tropezón plutonic complex intruded (Figure 15). We thus propose that the transition between AFS and TFS slip occurred between 114 and 107 Ma, the overlap in ages between prekinematic dikes and synkinematic calcite and plutonism (Figure 15). Both the Tropezón and the Librillo intrusive complexes are cut by faults pertaining to the TFS, which demonstrates that slip along these faults must have continued later than the 106–101 Ma intrusive age of the Librillo intrusive complex.

Bonson (1998) provides a model of mineralization evolution from high-temperature (300–500 ° C) magnetite-dominated deposits to moderate-temperature (130–390 °C) hematite-chalcopyrite (+calcite) mineralization. This switch in mineralization style is linked to a switch in structural control, such that the earlier mineralization is controlled by N striking AFS ductile and brittle structures, and the later mineralization is controlled by NW striking brittle faults. Many TFS faults in the area are mineralized with hematite and/or calcite; we use this observation in the context of the Bonson (1998) model to support our interpretation that there was not a protracted hiatus between AFS and TFS brittle deformation.

Cross-cutting relationships reveal that the El Muelle fault cuts Early Cretaceous volcanic rocks, but a younger age limit cannot be determined for this fault. The andesite dike mapped in Figure 6 cuts the easternmost strands of the AFS but is displaced by an AFS fault to the west (Figure 6). Valley alluvium prevents tracing this dike to the El Muelle fault, but we take the exposed relationship to tentatively suggest that brittle faulting transitioned westward across faults in the waning stages of AFS deformation, and the El Muelle fault may be the youngest AFS-connected fault. Curvature of the El Muelle fault toward parallelism with the Taltal fault is consistent with a coeval kinematic relationship. Moreover, the El Muelle fault is not displaced by TFS faults, including the Quebrada de la Peineta fault that offsets the eastern strand nearly 1 km. Following typical fault displacement-length scaling relationships for strike-slip faults (e.g., Clark & Cox, 1996; Kim & Sanderson, 2005), faults with ~1 km of displacement should be ~10–100 km long; we propose that the ~1 km offset on of the AFS eastern strand by the Quebrada de la Peineta fault is unlikely to have dissipated along strike at the intersection with the El Muelle fault, and instead these faults appear to have

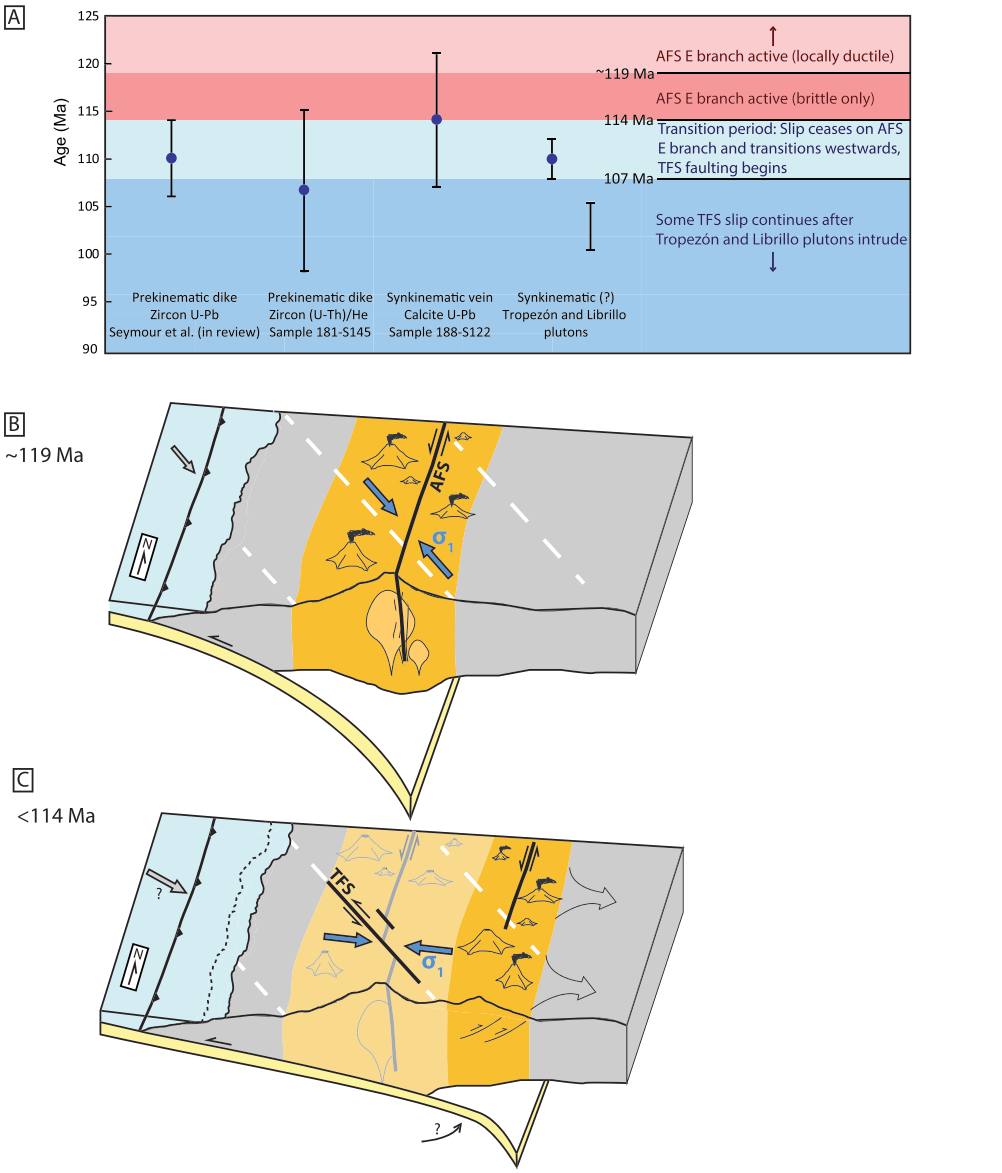

Figure 15. (a) Summary of timing constraints for the transition between AFS and TFS slip. The two dikes dated in this study are prekinematic to the TFS and late kinematic to the AFS. Calcite sample 188-S122 is along a TFS fault that postdates the AFS, and calcite mineralization is late kinematic to that fault. While the Tropezón and Librillo plutons (ages from Tornos et al., 2010 and Espinoza et al., 2014, respectively) are cut by TFS faults, they may have less sinistral offset than older units and are most likely synkinematic to the TFS. We bracket the AFS-TFS transition between the older limit of the andesitic dike date and the younger limit of the Tropezón pluton, similar to the younger limit of the calcite date. (b) Schematic model (not to scale) showing major tectonic features of northern Chile in the mid-Early Cretaceous. Margin-parallel shear is accommodated by the AFS in the rheologically weak Early Cretaceous arc (orange), with localized ductile deformation surrounding synkinematic plutons. Northwest striking inherited weaknesses (dashed white lines) are misoriented for reactivation by the NW-SE shortening regime in the study area (blue). (c) Schematic model showing abandonment and eastward migration of the arc beginning in the late Early Cretaceous. Northwest striking inherited weaknesses are favorably oriented for reactivation by the E-W shortening regime within the study area and offset the inactive arc and AFS (gray). Continued margin-parallel shear may be accommodated by strike-slip faults at the new arc axis (e.g., the transpressional Chivato fault system). Margin-orthogonal shortening away from northwest striking weaknesses could be accommodated by thrust faulting and basin inversion, uplifting the Coastal Cordillera and providing the sediment pulse (arrows) of the early Peruvian phase as described by Bascuñán et al. (2016). Possible changes to subduction dynamics such as slab shallowing, a change of subduction obliquity or rate, or a change in the margin position from subduction erosion are depicted schematically; additional factors such as a change in slab density or passage of a spreading center could explain the shift between major fault systems.

evolved contemporaneously. We interpret the apparent younging-westward pattern of AFS faults in conjunction with the curving trace of the El Muelle fault to indicate that slip on the TFS and El Muelle branch of the AFS temporally overlapped. With the possible exception of the El Muelle fault, we do not find evidence that TFS faults formed as secondary splay faults in duplex relationships to AFS faults, as documented with NW striking faults near Antofagasta (Cembrano et al., 2005; Jensen et al., 2011; Veloso et al., 2015). Instead, the TFS everywhere cross cuts and postdates the eastern strand and related strands of the AFS with no deflection of TFS fault traces near AFS fault intersections.

As there are no Late Cretaceous nor Paleogene map units in the region, and we have not identified any units that clearly postdate the entirety of displacement on the Taltal fault, the lower age limit of slip on the TFS is not well constrained. Arabasz (1971) described canyon incision and deposition of gravels in Quebrada Taltal after displacement on the Taltal fault had ceased; biotite K/Ar analyses of ash layers interbedded with these gravels give mid-Miocene dates (Escribano et al., 2013).

6.3. Relationship of TFS Kinematics to Cretaceous Plate Tectonics

Timing constraints presented above place TFS deformation after ~114–107 Ma and at least some of the deformation after 106–101 Ma, which shows that the main episode of TFS deformation followed abandonment of the AFS main strand as the region cooled and underwent a kinematic switch from NW-SE to E-W shortening. This timing shortly precedes or is contemporaneous with the mid-Cretaceous eastward migration of the magmatic arc (Dallmeyer et al., 1996), and no plutonism is recorded in the study area after ~101 Ma. This shift likewise appears contemporaneous with regional shortening and uplift; Late Cretaceous NW-SE or E-W shortening is described inland of the AFS at latitude 27°S (Mpodozis & Allmendinger, 1993), E-W crustal shortening of the Chilean Coastal Cordillera has been reported at latitude 32°S at ~100 Ma (Arancibia, 2004), and a widespread Albian-Cenomanian unconformity across the northern Andes is interpreted to reflect compression during plate reorganization (Jaimes & Freitas, 2006). The middle member of the Cretaceous Tonel formation in the Salar de Atacama basin records pulses of sedimentation derived from the west interpreted to reflect uplift of the Coastal Cordillera beginning around 107 Ma (Bascuñán et al., 2016); internal unconformities and growth strata show deposition in a compressional tectonic regime alongside an east vergent thrust (Arriagada et al., 2006; Mpodozis et al., 2005). The similar timing of the switch between AFS and TFS fault systems and an increase of retroarc foredeep sedimentation suggests a widespread shift in the location and style of deformation. This transition could reflect a margin-wide tectonic shift attributed to the southward passage of the Farallon-Phoenix-South America triple junction along the Chilean margin (Scheuber et al., 1994), slab flattening followed by breakoff (Haschke et al., 2002), or a 105–100 Ma global plate reorganization and change in seafloor spreading rates (Matthews et al., 2012). Alternatively, this transition may reflect a change in the loci of strain partitioning such that margin-orthogonal component of oblique convergence was accommodated in the study area while the margin-parallel component shifted east of the Coastal Cordillera. While data presented in this study cannot distinguish between these factors, they demonstrate that deformation of the TFS was contemporaneous with these changes. Regardless of the tectonic drivers of this transition, transfer of slip from the AFS to the TFS in the late Early Cretaceous represented a major shift in the structural evolution of the Coastal Cordillera. While some TFS slip postdates the late Early Cretaceous Tropezón and Librillo plutonic complexes, models that invoke Eocene slip on TFS faults must reconcile with the relationships described in this study that show most slip occurring before intrusion of those plutons.

7. Conclusions

The TFS consists of vertical to steeply NE dipping faults with 10.6 km total sinistral separation across a 15-km wide zone and 7.5 km sinistral slip on the largest fault. Collocation of TFS faults with aeromagnetic lineaments and abrupt changes in the thickness of Jurassic sedimentary strata suggest that they reactivated crustal anisotropies inherited from Paleozoic or earlier Mesozoic tectonism. Dates of a calcite vein (141 ± 11 Ma) and rhyolite dike ~146 Ma emplaced along the Taltal fault indicate that the TFS controlled fluid flow and magmatism as early as the Late Jurassic, prior to displacement on the AFS and subsequent TFS. However, geologic mapping indicates the TFS records little to no pre- or syn-AFS sinistral slip. Geochronology of dikes and veins with prekinematic and synkinematic relationships to the TFS demonstrates that the transition between AFS and TFS brittle deformation occurred between ~114 and 107 Ma

(Figure 15). The ~110 Ma Tropezón plutonic complex records distributed sinistral shear along the splaying eastward termination of the Taltal fault. The 106–101 Ma Librillo plutonic complex is likewise cut by TFS faults, demonstrating that at least some slip on the TFS occurred after that time. The transition between these fault systems records a switch from a NW-SE to E-W shortening regime, which most likely reflects either a margin-wide shift in convergence direction or a shift in strain partitioning such that margin-parallel deformation was accommodated further east, and margin-orthogonal shortening along preexisting NW striking weak zones was accommodated in the Coastal Cordillera.

Acknowledgments
Analytical costs for this project were funded in part by the Geological Society of America student research grant to S. Mavor and by the National Science Foundation grant 1822064 to J. Singleton. We thank Micah Hernandez for field assistance and sample preparation and thank Gabriela Bórquez G. for field assistance. Data for table S1 are on the Strabospot database of structural measurements here: https://www.strabospot.org/search/ Data for tables S2 and S3(zircon U-Pb and (U-Th)/He) are here: https://www.geochron.org/dataset/html/geochron_dataset_2020_01_26_XRJ5H Data for table S4 (Calcite U-Pb) are here: https://www.geochron.org/results.php?pkey=28356

References

Abels, A., & Bischoff, L. (1999). Clockwise block rotations in northern Chile: Indications for a large-scale domino mechanism during the middle-late Eocene. *Geology*, *27*(8), 751–754. https://doi.org/10.1130/0091-7613(1999)027<0751:CBRINC>2.3.CO;2

Allmendinger, R. W., Cardozo, N., & Fisher, D. M. (2011). Structural geology algorithms. In Structural geology algorithms: Vectors and Tensors (Vol. 9781107012). https://doi.org/10.1017/CBO9780511920202

Álvarez, J., Jorquera, R., Miralles, C., Padel, M., & Martinez, P. (2016). *Cartas Punta Posallaves y Sierra Vicuña Mackenna, Región de Antofagasta. (Carta Geológica de Chile, Serie Geología Básica 183-184 scale 1: 100.000)*. Santiago: Servicio Nacional de Geología y Minería.

Angermann, D., Klotz, J., & Reigber, C. (1999). Space-geodetic estimation of the Nazca-South America Euler vector. *Earth and Planetary Science Letters*, *171*(3), 329–334. https://doi.org/https://doi.org/10.1016/S0012-821X(99)00173-9

Arabasz, W. (1968). Geologic structure of the Taltal Area, northern Chile, in relation to the earthquake of December 28, 1966. *Bulletin of the Seismological Society of America*, *58*(3), 835–842.

Arabasz, W. J. J. (1971). Geological and Geophysical studies of the Atacama fault zone in northern Chile, (Doctoral dissertation). Retrived from CaltechTHESIS. (http://resolver.caltech.edu/CaltechTHESIS:02092018-150208279). Pasadena: California Institute of Technology.

Arancibia, G. (2004). Mid-Cretaceous crustal shortening: Evidence from a regional-scale ductile shear zone in the Coastal Range of central Chile (32° S). *Journal of South American Earth Sciences*, *17*(3), 209–226. https://doi.org/10.1016/j.jsames.2004.06.001

Arriagada, C., Cobbold, P. R., & Roperch, P. (2006). Salar de Atacama basin: A record of compressional tectonics in the central Andes since the mid-Cretaceous. *Tectonics*, *25*, TC1008. https://doi.org/10.1029/2004TC001770

Bascuñán, S., Arriagada, C., Le Roux, J., & Deckart, K. (2016). Unraveling the Peruvian phase of the central Andes: Stratigraphy, sedimentology and geochronology of the Salar de Atacama basin (22°30–23°S), northern Chile. *Basin Research*, *28*(3), 365–392. https://doi.org/10.1111/bre.12114

Bell, C. M. (1982). The Lower Paleozoic metasedimentary basement of the Coastal Ranges of Chile between 25 30′ and 27 S. *Revista Geologica de Chile*, *17*, 21–24.

Bell, C. M. (1984). Deformation produced by the subduction of a Palaeozoic turbidite sequence in northern Chile. *Journal of the Geological Society*, *141*(2), 339–347. https://doi.org/10.1144/gsjgs.141.2.0339

Bell, C. M. (1987). The origin of the Upper Palaeozoic Chañaral melange of N Chile. *Journal of the Geological Society*, *144*(4), 599–610.

Bonson, C. G. (1998). Fracturing, fluid processes and mineralisation in the Cretaceous continental magmatic arc of northern Chile (25° 15′-27° 15′S), (Doctoral dissertation). Retrived from EThOS. (https://ethos.bl.uk/OrderDetails.do?uin=uk.bl.ethos.310616). London: Kingston University.

Brown, M., Diaz, F., & Grocott, J. (1993). Displacement history of the Atacama fault system 25°00′S-27°00′S, northern Chile. *Geological Society of America Bulletin*, *105*(9), 1165–1174. https://doi.org/10.1130/0016-7606(1993)105<1165:DHOTAF>2.3.CO;2

Cardozo, N., & Allmendinger, R. W. (2013). Spherical projections with OSXStereonet. *Computers and Geosciences*, *51*, 193–205. https://doi.org/10.1016/j.cageo.2012.07.021

Cembrano, J., González, G., Arancibia, G., Ahumada, I., Olivares, V., & Herrera, V. (2005). Fault zone development and strain partitioning in an extensional strike-slip duplex: A case study from the Mesozoic Atacama fault system, northern Chile. *Tectonophysics*, *400*(1–4), 105–125. https://doi.org/10.1016/j.tecto.2005.02.012

Charrier, R., Pinto, L., & Rodríguez, M. P. (2007). Tectonostratigraphic evolution of the Andean orogen in Chile. In The geology of Chile. https://doi.org/10.1144/GOCH.3

Clark, R. M., & Cox, S. J. D. (1996). A modern regression approach to determining fault displacement-length scaling relationships. *Journal of Structural Geology*, *18*(2), 147–152. https://doi.org/https://doi.org/10.1016/S0191-8141(96)80040-X

Coira, B., Davidson, J., Mpodozis, C., & Ramos, V. (1982). Tectonic and magmatic evolution of the Andes of northern Argentina and Chile. *Earth Science Reviews*, *18*(3–4), 303–332. https://doi.org/10.1016/0012-8252(82)90042-3

Contreras, J. P., Espinoza, M., De la Cruz, R., Jorquera, R., Kraus, S., Ramírez, C., et al. (2013). *Carta Cifuncho, Regiones de Antofagasta y Atacama. (Carta Geológica de Chile, Serie Geología Básica, 161)*. Santiago: Servicio Nacional de Geología y Minería.

Contreras, Juan Pablo. (2018). Segmentación de patrones de rotación tectónica delimitados por la falla Taltal: Cordillera de la Costa del Norte de Chile (25°-26° Latitud Sur), (Master's thesis). Retrived from the Repositorio Académico de la Universidad de Chile. (http://repositorio.uchile.cl/handle/2250/159307). Santiago: Universidad de Chile.

Dallmeyer, D., Brown, M., Grocott, J., Taylor, G. K., & Treloar, P. (1996). Mesozoic magmatic and tectonic events within the Andean plate boundary zone, north Chile. *Journal of Geology*, *104*(1), 19–40.

Escribano, J., Martínez, P., Domagala, J., Padel, M., Espinoza, M., Jorquera, R., et al. (2013). *Cartas Bahía Isla Blanca y Taltal, Región de Antofagasta. (Carta Geológica de Chile, Serie Geología Básica, 164–165, scale 1:100,000)*. Santiago: Servicio Nacional de Geología y Minería.

Espinoza, M., Contreras, J. P., Jorquera, R., De La Cruz, R., Kraus, S., & Ramírez, C. (2014). *Carta Cerro del Pingo, Regiones de Antofagasta y Atacama. (Carta Geológica de Chile, Serie Geología Básica 169, scale 1:100.000)*. Santiago: Servicio Nacional de Geología y Minería.

Fuentes, P., Díaz-Alvarado, J., Fernández, C., Díaz-Azpiroz, M., & Rodríguez, N. (2016). Structural analysis and shape-preferred orientation determination of the mélange facies in the Chañaral mélange, Las Tórtolas Formation, Coastal Cordillera, northern Chile. *Journal of South American Earth Sciences*, *67*, 40–56. https://doi.org/10.1016/j.jsames.2016.02.001

Grocott, J., Brown, J., Dallmeyer, R. D., Taylor, G. K., & Treloar, P. J. (1994). Mechanism of continental growth in extensional arcs: An exemple from the Andean plate boundary zone. *Geology*, *22*, 391–394. https://doi.org/10.1130/0091-7613(1994)022<0391:MOCGIE>2.3.CO;2

Grocott, J., & Taylor, G. K. (2002). Magmatic arc fault systems, deformation partitioning and emplacement of granitic complexes in the Coastal Cordillera, north Chilean Andes (25°30′S to 27°00′S). *Journal of the Geological Society*, *159*(4), 425–443. https://doi.org/10.1144/0016-764901-124

Guynn, J., & Gehrels, G. (2010). Comparison of detrital zircon age distributions using the K-S test. Manual, (c), 1–16.

Haschke, M. R., Scheuber, E., Günther, A., & Reutter, K.-J. (2002). Evolutionary cycles during the Andean orogeny: Repeated slab breakoff and flat subduction? *Terra Nova*, *14*(1), 49–55. https://doi.org/10.1046/j.1365-3121.2002.00387.x

Hill, C. A., Polyak, V. J., Asmerom, Y., & Provencio, P. (2016). Constraints on a Late Cretaceous uplift, denudation, and incision of the Grand Canyon region, southwestern Colorado Plateau, USA, from U-Pb dating of lacustrine limestone. *Tectonics*, *35*, 896–906. https://doi.org/10.1002/2016TC004166

Holdsworth, R. E., Butler, C. A., & Roberts, A. M. (1997). The recognition of reactivation during continental deformation. *Journal of the Geological Society*, *154*(1), 73–78. https://doi.org/10.1144/gsjgs.154.1.0073

Jaimes, E., & Freitas, M. (2006). An Albian–Cenomanian unconformity in the northern Andes: Evidence and tectonic significance. *Journal of South American Earth Sciences*, *21*, 461–492. https://doi.org/10.1016/j.jsames.2006.07.011

Jensen, E., Cembrano, J., Faulkner, D., Veloso, E., & Arancibia, G. (2011). Development of a self-similar strike-slip duplex system in the Atacama fault system, Chile. *Journal of Structural Geology*, *33*(11), 1611–1626. https://doi.org/10.1016/j.jsg.2011.09.002

Kim, Y.-S., & Sanderson, D. J. (2005). The relationship between displacement and length of faults: A review. *Earth-Science Reviews*, *68*(3), 317–334. https://doi.org/https://doi.org/10.1016/j.earscirev.2004.06.003

Kylander-Clark, A. R. C., Hacker, B. R., & Cottle, J. M. (2013). Laser-ablation split-stream ICP petrochronology. *Chemical Geology*, *345*, 99–112. https://doi.org/https://doi.org/10.1016/j.chemgeo.2013.02.019

Ludwig, K. R. (2003). User's manual for Isoplot 3.00: A geochronological toolkit for Microsoft Excel. Berkeley Geochronology Center, Special Publication, 4, 25–32.

Marrett, R., & Allmendinger, R. W. (1990). Kinematic analysis of fault-slip data. *Journal of Structural Geology*, *12*(8), 973–986. https://doi.org/10.1016/0191-8141(90)90093-E

Marsh, J. H., & Stockli, D. F. (2015). Zircon U–Pb and trace element zoning characteristics in an anatectic granulite domain: Insights from LASS-ICP-MS depth profiling. *Lithos*, *239*, 170–185. https://doi.org/https://doi.org/10.1016/j.lithos.2015.10.017

Mason, A. J., Henderson, G. M., & Vaks, A. (2013). An acetic acid-based extraction protocol for the recovery of U, Th and Pb from calcium carbonates for U-(Th)-Pb geochronology. *Geostandards and Geoanalytical Research*, *37*(3), 261–275. https://doi.org/10.1111/j.1751-908X.2013.00219.x

Matthews, K. J., Seton, M., & Müller, R. D. (2012). A global-scale plate reorganization event at 105–100 Ma. *Earth and Planetary Science Letters*, *355–356*, 283–298. https://doi.org/https://doi.org/10.1016/j.epsl.2012.08.023

Moore, J. C. (1978). Orientation of underthrusting during latest Cretaceous and earliest Tertiary time, Kodiak Islands, Alaska. *Geology*, *6*(4), 209–213. https://doi.org/10.1130/0091-7613(1978)6<209:OOUDLC>2.0.CO;2

Mpodozis, C., & Allmendinger, R. W. (1993). Extensional tectonics, Cretaceous Andes, northern Chile (27°S). *GSA Bulletin*, *105*(11), 1462–1477. https://doi.org/10.1130/0016-7606(1993)105<1462:ETCANC>2.3.CO;2

Mpodozis, C., Arriagada, C., Basso, M., Roperch, P., Cobbold, P. R., & Reich, M. (2005). Late Mesozoic to Paleogene stratigraphy of the Salar de Atacama Basin, Antofagasta, northern Chile: Implications for the tectonic evolution of the central Andes. *Tectonophysics*, *399*, 125–154. https://doi.org/10.1016/j.tecto.2004.12.019

Naranjo, J. A., & Puig, A. (1984). *Hojas Taltal y Chanaral, regiones de Antofagasta y Atacama. (Cartas geologicas de Chile 62-63, scale 1:250,000)*. Santiago: Servicio Nacional de Geología y Minería.

Nuriel, P., Weinberger, R., Kylander-Clark, A. R. C., Hacker, B. R., & Craddock, J. P. (2017). The onset of the Dead Sea transform based on calcite age-strain analyses. *Geology*, *45*(7), 587–590. https://doi.org/10.1130/G38903.1

Parada, M. A., López-Escobar, L., Oliveros, V., Fuentes, F., Morata, D., Calderón, M., et al. (2007). Andean magmatism. In T. Moreno & W. Gibbons (Eds.), *The Geology of Chile* (pp. 115–146). London, UK: The Geological Society. https://doi.org/10.1144/GOCH.4

Petit, J. P. (1987). Criteria for the sense of movement on fault surfaces in brittle rocks. *Journal of Structural Geology*, *9*(5), 597–608. https://doi.org/https://doi.org/10.1016/0191-8141(87)90145-3

Prinz, P., Wilke, H.-G., & von Hillebrandt, A. (1994). Sediment accumulation and subsidence history in the Mesozoic marginal basin of northern Chile. In K.-J. Reutter, E. Scheuber, & P. J. Wigger (Eds.), *Tectonics of the Southern Central Andes* (pp. 219–232). Berlin, Heidelberg: Springer. https://doi.org/10.1007/978-3-642-77353-2_15

Randall, D. E., Taylor, G. K., & Grocott, J. (1996). Major crustal rotations in the Andean margin: Paleomagnetic results from the Coastal Cordillera of northern Chile. *Journal of Geophysical Research*, *101*(B7), 15,783–15,798. https://doi.org/10.1029/96JB00817

Reiners, P. W., Farley, K. A., & Hickes, H. J. (2002). He diffusion and (U–Th)/He thermochronometry of zircon: Initial results from Fish Canyon Tuff and Gold Butte. *Tectonophysics*, *349*(1), 297–308. https://doi.org/10.1016/S0040-1951(02)00058-6

Reiners, P. W., Spell, T. L., Nicolescu, S., & Zanetti, K. A. (2004). Zircon (U-Th)/He thermochronometry: He diffusion and comparisons with 40Ar/39Ar dating. *Geochimica et Cosmochimica Acta*, *68*(8), 1857–1887. https://doi.org/10.1016/j.gca.2003.10.021

Roberts, N. M. W., Rasbury, E. T., Parrish, R. R., Smith, C. J., Horstwood, M. S. A., & Condon, D. J. (2017). A calcite reference material for LA-ICP-MS U-Pb geochronology. *Geochemistry, Geophysics, Geosystems*, *18*, 2807–2814. https://doi.org/10.1002/2016GC006784

Ruthven, R. C., Singleton, J. S., Seymour, N. M., Gomila, R., Arancibia, G., Stockli, D. F., et al. (2020). The geometry, kinematics, and timing of deformation along the southern segment of the Paposo fault zone, Atacama fault system, northern Chile. *Journal of South American Earth Sciences*, *97*. https://doi.org/10.1016/j.jsames.2019.102355

Salfity, J. (1985). Lineamientos transversales al rumbo andino en el noroeste argentino. Paper presented at 4th Congreso Geológico Chileno, Antofagasta, Chile.

Scheuber, E. (1994). Jurassic-Early Cretaceous mafic dikes from north Chilean Coastal Cordillera (23°–25°): Indicators for extension and paleostress. Paper presented at 7th Congreso Geológico Chileno, Concepción, Chile.

Scheuber, E., & Andriessen, P. A. M. (1990). The kinematic and geodynamic significance of the Atacama fault zone, northern Chile. *Journal of Structural Geology*, *12*(2), 243–257. https://doi.org/10.1016/0191-8141(90)90008-M

Scheuber, E., Bogdanic, T., Jensen, A., & Reutter, K.-J. (1994). Tectonic development of the north Chilean Andes in relation to plate convergence and magmatism since the Jurassic. In K.-J. Reutter, E. Scheuber, & P. J. Wigger (Eds.), *Tectonics of the southern central Andes*, (pp. 121–139). Berlin, Heidelberg: Springer. https://doi.org/10.1007/978-3-642-77353-2_9

Scheuber, E., & Gonzalez, G. (1999). Tectonics of the Jurassic-Early Cretaceous magmatic arc of the north Chilean Coastal Cordillera (22°-26°S): A story of crustal deformation along a convergent plate boundary. *Tectonics*, *18*(5), 895–910. https://doi.org/10.1029/1999TC900024

Seymour, N. M., Singleton, J. S., Mavor, S. P., Gomila, R., Stockli, D. F., Heuser, G., & Arancibia, G. (2020). The relationship between magmatism and deformation along the intra-arc strike-slip Atacama fault system, northern Chile. *Tectonics*, *39*, e2019TC005702. https://doi.org/10.1029/2019TC005702

Seymour, N. M., Stockli, D. F., Beltrando, M., & Smye, A. J. (2016). Tracing the thermal evolution of the Corsican lower crust during Tethyan rifting. *Tectonics*, *35*, 2439–2466. https://doi.org/10.1002/2016TC004178

Suarez, M., & Bell, C. M. (1992). Triassic rift-related sedimentary basins in northern Chile (24°–29°S). *Journal of South American Earth Sciences*, *6*(3), 109–121. https://doi.org/10.1016/0895-9811(92)90001-F

Tankard, A. J., Uliana, M. A., Welsink, H. J. J., Ramos, V. A., Tunik, M., Franca, A. B., et al. (1995). Structural and tectonic controls of basin evolution in southwestern Gondwana during the Phanerozoic. In A. J. Tankard, R. S. Soruco, & H. J. Welsink (Eds.), Petroleum Basins of South America: AAPG Memoir 62 (p. 0). https://doi.org/10.1306/M62593C1

Taylor, G. K., Grocott, J., Pope, A., & Randall, D. E. (1998). Mesozoic fault systems, deformation and fault block rotation in the Andean forearc: A crustal scale strike-slip duplex in the Coastal Cordillera of northern Chile. *Tectonophysics*, *299*(1–3), 93–109. https://doi.org/10.1016/S0040-1951(98)00200-5

Tornos, F., Velasco, F., Barra, F., & Morata, D. (2010). The Tropezón Cu-Mo-(Au) deposit, northern Chile: The missing link between IOCG and porphyry copper systems? *Mineralium Deposita*, *45*(4), 313–321. https://doi.org/10.1007/s00126-010-0277-8

Ulriksen, C. (1979). Regional geology, geochronology and metallogeny of the Coastal Cordillera of Chile between 25°30′ and 26°00′ south, (Master's thesis). Retrieved from DalSpace. (http://hdl.handle.net/10222/75332). Halifax: Dalhousie University.

Vaks, A., Woodhead, J., Bar-Matthews, M., Ayalon, A., Cliff, R. A., Zilberman, T., et al. (2013). Pliocene–Pleistocene climate of the northern margin of Saharan–Arabian Desert recorded in speleothems from the Negev Desert, Israel. *Earth and Planetary Science Letters*, *368*, 88–100. https://doi.org/https://doi.org/10.1016/j.epsl.2013.02.027

Veloso, E. E., Gomila, R., Cembrano, J., González, R., Jensen, E., & Arancibia, G. (2015). Stress fields recorded on large-scale strike-slip fault systems: Effects on the tectonic evolution of crustal slivers during oblique subduction. *Tectonophysics*, *664*, 244–255. https://doi.org/10.1016/j.tecto.2015.09.022

Vermeesch, P. (2012). On the visualisation of detrital age distributions. *Chemical Geology*, *312–313*, 190–194. https://doi.org/https://doi.org/10.1016/j.chemgeo.2012.04.021

Vivallos, J., & Donoso, C. (2014a). *Carta magnética Cerro del Pingo, regiones de Antofagasta y Atacama. (Carta Geológica de Chile, Serie Geofisica 83, scale 1:100,000)*. Santiago: Servicio Nacional de Geología y Minería.

Vivallos, J., & Donoso, C. (2014b). *Carta magnética Cifuncho, region de Antofagasta. (Carta Geológica de Chile, Serie Geofisica 81, scale 1:100,000)*. Santiago: Servicio Nacional de Geología y Minería.

Vivallos, J., & Donoso, C. (2014c). *Cartas magnéticas Bahía Isla Blanca y Taltal, region de Antofagasta. (Carta Geológica de Chile, Serie Geofisica 73-74, scale 1:100,000)*. Santiago: Servicio Nacional de Geología y Minería.

Wilson, J., Dallmeyer, R. D. R., & Grocott, J. (2000). New 40Ar/39Ar dates from the Las Tazas complex, northern Chile: Tectonic significance. *Journal of South American Earth Sciences*, *13*(1), 115–122. https://doi.org/10.1016/S0895-9811(00)00008-0

Wolfe, M. R., & Stockli, D. F. (2010). Zircon (U–Th)/He thermochronometry in the KTB drill hole, Germany, and its implications for bulk He diffusion kinetics in zircon. *Earth and Planetary Science Letters*, *295*(1), 69–82. https://doi.org/https://doi.org/10.1016/j.epsl.2010.03.025